Three-dimensional Simulation of Unstable Gravity-driven Infiltration of Water into a Porous Medium

Hector Gomez[1*], Luis Cueto-Felgueroso[2*], Ruben Juanes[2*]

1: University of A Coruña
Campus de Elviña s/n,
15192, A Coruña, Spain.
2: Massachusetts Institute of Technology
77 Massachusetts Avenue,
Cambridge, MA 02139, USA.

Abstract

Infiltration of water in dry porous media is subject to a powerful gravity-driven instability. Although the phenomenon of unstable infiltration is well known, its description using continuum mathematical models has posed a significant challenge for several decades. The classical model of water flow in the unsaturated flow, the Richards equation, is unable to reproduce the instability. Here, we present a computational study of a model of unsaturated flow in porous media that extends the Richards equation and is capable of predicting the instability and captures the key features of gravity fingering quantitatively. The extended model is based on a phase-field formulation and is fourth-order in space. The new model poses a set of challenges for numerical discretizations, such as resolution of evolving interfaces, stiffness in space and time, treatment of singularly perturbed equations, and discretization of higher-order spatial partial-differential operators. We develop a numerical algorithm based on Isogeometric Analysis, a generalization of the finite element method that permits the use of globally-smooth basis functions, leading to a simple and efficient discretization of higher-order spatial operators in variational form. We illustrate the accuracy, efficiency and robustness of our method with several examples in two and three dimensions in both homogeneous and strongly heterogeneous media. We simulate, for the first time, unstable gravity-driven infiltration in three dimensions, and confirm that the new theory reproduces the fundamental features of water infiltration into a porous medium. Our results are consistent with classical experimental observations that demonstrate a transition from stable to unstable fronts depending on the infiltration flux.

Keywords: Phase-field, Infiltration, Gravity Fingering, Isogeometric Analysis

1. Introduction

Infiltration of water in soil is an essential component of the hydrologic cycle. Rainfall water that infiltrates the soil recharges groundwater resources and sustains the vegetation and soil biota. The dynamics of water in the unsaturated zone is therefore a key to understand the interplay between climate, soil moisture and vegetation in water-stressed ecosystems [68]. Infiltration has been modeled using a variety of approaches, depending on the scale and scope of the investigation. These range from zero-dimensional "bucket" models to the classical Richards equation: a partial differential equation that describes the evolution of water content in space and time through and extension of the Darcy-Buckingham flux model to unsaturated media [8].

*Corresponding author
Email address: hgomez@udc.es (Hector Gomez[1])

Gravity-driven wetting fronts are often unstable, leading to a phenomenon known as "gravity fingering": water infiltrates the soil through preferential flow paths rather than as compact wetting front [40, 41, 42, 48, 78]. These paths appear as columnar channels, through which water penetrates into the soil much faster than predicted by the Richards equation. Fingering is a powerful hydrodynamic instability, ubiquitous in both homogeneous and heterogeneous dry soils, and may be the prevalent infiltration form in arid and semi-arid environments. Remarkably, the fingering instability is not predicted by the classical theory [33]. Richards' equation is a scalar conservation law expressing conservation of mass, which takes the form of a second order, nonlinear advection-diffusion equation. It has been shown that Richards' equation is stable in homogeneous soil against both infinitesimal and finite perturbations [37, 63]. Models of unsaturated flow capable of describing unstable flows require the introduction of higher-order effects, either resorting to hysteresis and dynamic effects in the capillary pressure function [33, 63], or through the introduction of an effective macroscopic surface tension in the mathematical description of unsaturated flow [24, 25]. Here we focus on this latter approach. Mathematically, we adopt a phase field formulation, where a square-gradient term in the energy appears naturally, and leads to a fourth-order term in the mass conservation equation [17]. Previous work in two dimensions has shown that the model predicts gravity fingering, and the results of the linear stability analysis agree well with laboratory experiments in terms of finger width and finger velocity [24, 25].

Here we present a computational study of unstable infiltration, based on a fourth-order phase-field model of unsaturated flow. The numerical simulation of conservation laws with fourth-order terms is challenging. Classical examples of such models are the Cahn-Hilliard phase-field model of phase separation [17], the Kuramoto-Sivashinsky equation [56, 72] and the long-wave thin film equation [52]. Most numerical methodologies for the approximation of partial-differential equations have been developed for equations involving second (or lower)-order operators, yet fourth-order equations are receiving increased attention, primarily due to the fast development of phase-field models [1, 15, 16, 17, 18] of fracture mechanics [11, 79, 67], multiphase flow [54, 55, 62, 76] and tumor growth [9, 23, 61, 64, 80]. The development of accurate, robust, and efficient algorithms for these problems has become a necessity.

Computational phase-field modeling has been traditionally dominated by collocation methods, such as finite differences [36, 74, 25] or pseudo-spectral algorithms [57, 60, 81, 28], by finite volume schemes [27], and by mixed finite element methods [3, 10, 31, 35]. Since our model equation involves fourth-order partial derivatives, conforming finite element formulations require $\mathcal{C}^1$ continuity of the basis functions across element boundaries. The design of simple, efficient and geometrically flexible finite elements possessing global $\mathcal{C}^1$ continuity has been a prime objective of the finite element community for several decades [73]. Although significant progress has been made, most existing procedures require the introduction of additional global degrees of freedom and entail theoretical and computational difficulties. In fact, most finite element computations of fourth-order equations are performed using a mixed method, which doubles the number of global unknowns and may require a theoretical study of the space stability of the discretization. Here, we employ a numerical formulation based on Isogeometric Analysis, a technology that has been recently introduced in the field of computational mechanics [20, 51]. Isogeometric Analysis may be thought of as a class of isoparametric finite element analysis in which the basis functions in the parameter space are Non-Uniform

Rational B-Splines (NURBS) [65, 69]. NURBS are a superset of piecewise polynomials, which ensures that Isogeometric Analysis is a generalization of finite element analysis. For the purpose of this work, the most important advantage of Isogeometric Analysis is that, in contrast with classical finite element methods, it permits building globally $\mathcal{C}^1$ continuous basis functions in a simple and efficient way. Additional advantages of Isogeometric Analysis over the finite element method that are relevant to the infiltration problem are, for example, enhanced spectral accuracy (i.e., approximability of the method for discrete eigenvalue problems) [14, 22, 50], and superior robustness (i.e., balance between accuracy and dissipation properties of the method for stiff nonlinear dynamic problems) [2, 4, 32, 34, 45, 46, 59]. Our methodology also presents advantages over other numerical methods often used for fourth-order equations. For example, our method is very flexible with respect to the geometry of the domain, in contrast with spectral methods which are difficult to apply to complex geometries. Another frequently used method, the finite volume method, does have geometrical flexibility but studies of theoretical nature regarding convergence and/or stability are usually more intricate than those of finite element procedures based on the weak form of the problem.

In summary, our manuscript presents the first three-dimensional simulations of unstable gravity-driven infiltration. Until now, it was unclear whether three-dimensional unstable infiltration could be captured with a continuum mathematical theory. Our simulations elucidate important aspects of the physics of the problem, which had so far remained elusive to continuum modeling. For example, the hydrodynamic instability develops a columnar pattern in three dimensions; and the instability is suppressed for high infiltration rates. We also analyze, for the first time, the impact of heterogeneous permeability on the infiltration patterns. We propose a computational method that is especially well-suited for simulating this problem, the reasons being that: (1) our method permits generating globally C^1 continuous basis functions which are essential to solve a fourth-order partial differential equation in primal variational form; and (2) our method exhibits improved spectral accuracy, a property that plays a critical role in the solution of nonlinear dynamic problems like the one studied here.

The outline of the paper is as follows: In section 2 we present the governing equations of our model of water infiltration in soil. In section 3, we present the numerical algorithms used to approximate the solution of the infiltration equation. In section 4 we present several numerical examples in two and three dimensions. Finally, we draw conclusions in section 5.

2. Governing equations

Unsaturated flow is traditionally modeled at the continuum scale through a balance equation for the mass of the infiltrating fluid, as follows

$$\frac{\partial\left(\rho\phi S\right)}{\partial t}+\nabla\cdot\mathbf{q}=0, \tag{1}$$

where ρ is the fluid density, ϕ the porosity of the medium, and S is the fluid saturation, that is the volumetric fraction of pore space occupied by the fluid. The mass flux, $\mathbf{q}$, is modeled through an extension of Darcy's law to partially saturated media

$$\mathbf{q}=-\rho\frac{k(\boldsymbol{x})}{\mu}k_r(S)\nabla\Phi, \tag{2}$$

where k is the permeability of the porous medium, μ is the dynamic viscosity of the fluid, k_r is the saturation-dependent relative permeability, and Φ is the flow potential. In the classical theory of unsaturated flow (Richards' equation [66]), the potential Φ is a function of fluid saturation alone. In contrast, we interpret the flow potential as the variational derivative of a phenomenological free energy functional, $\mathcal{E}$, as $\Phi = \dfrac{\delta \mathcal{E}}{\delta S}$. We propose to use [24]

$$\mathcal{E} = -\rho g z S + \Psi(S) + \frac{1}{2}\Gamma \left|\nabla S\right|^2, \tag{3}$$

where g is the acceleration due to gravity, z is depth (coordinate in the direction of gravity), and Ψ is a suction potential energy that scales with surface tension and medium permeability as $\Psi = -\dfrac{\gamma}{\sqrt{k}}\Psi_D(S)$ [58]. The dimensionless function $\Psi_D(S)$ is a convex nonlinear function of fluid saturation that achieves a local minimum within the interval [0,1]. In particular, we consider a two-parameter family of functions of the form [25]

$$\Psi_D(S) = \frac{\lambda}{\lambda - 1} S^{1-1/\lambda}\left[1 - e^{\kappa(S-1)}\right], \tag{4}$$

which is an extension of traditional Brooks-Corey capillary pressure functions [8] to ensure that $S \in [0, 1]$. The local minimum is reached for a value of the saturation that tends to one as κ tends to infinity. In the free energy (3), the square-gradient term is introduced to model an effective macroscopic surface tension [24]. This gradient energy seems to be essential to capture unstable, gravity-driven wetting fronts in unsaturated flow [24, 25]. Taking the variational derivative of (3) with respect to saturation yields the flow potential Φ, as

$$\Phi = \frac{\delta \mathcal{E}}{\delta S} = \frac{\partial \mathcal{E}}{\partial S} - \nabla \cdot \left(\frac{\partial \mathcal{E}}{\partial \nabla S}\right) = -\rho g z + \frac{d\Psi}{dS} - \Gamma \nabla^2 S, \tag{5}$$

where

$$\frac{d\Psi}{dS} = -\frac{\gamma}{\sqrt{k}}\frac{d\Psi_D}{dS} = -\frac{\gamma}{\sqrt{k}} J(S), \tag{6}$$

and we have introduced the notation $\dfrac{d\Psi_D}{dS} \equiv J(S)$. Based on the flow potential (5), the mass flux (2) is given by

$$\mathbf{q} = -\rho \frac{k(\boldsymbol{x})}{\mu} k_r(S)\left(-\rho g z - \frac{\gamma}{\sqrt{k}} J(S) - \Gamma \nabla^2 S\right). \tag{7}$$

Finally, assuming an incompressible fluid, our model equation expressing conservation of mass reads

$$\phi \frac{\partial S}{\partial t} + \nabla \cdot \left[\frac{\rho g}{\mu} k(\boldsymbol{x}) k_r(S) \nabla \left(z + \frac{\gamma}{\rho g \sqrt{k}} J(S) + \frac{\Gamma}{\rho g}\nabla^2 S\right)\right] = 0. \tag{8}$$

Note that the classical Richards model is recovered by setting $\Gamma = 0$ in the above equation. The above model is valid as long as the medium remains unsaturated (S strictly less than 1), and under the assumption that the mobility and compressibility of air are much larger than those of water.

2.1. Scalings and dimensionless model equation

Let us start by considering a homogeneous porous medium, where the porosity ϕ and the permeability k are constant throughout the domain, k. We define the saturated hydraulic conductivity as

$$K_{\text{sat}} = \frac{\rho g k}{\mu}, \tag{9}$$

which has units of velocity $[LT^{-1}]$. Defining the characteristic time as

$$t_c = \frac{\phi L}{K_{\text{sat}}}, \tag{10}$$

we may write the dimensionless counterpart of our model (8), as

$$\frac{\partial S}{\partial t} + \nabla \cdot \left[k_r(S) \nabla \left(z_D + N_{\text{Gr}}^{-1} J(S) + N_\Gamma \nabla^2 S \right) \right] = 0, \tag{11}$$

where we have abused notation and used $\boldsymbol{x}$ and t to denote dimensionless space and time. Two dimensionless groups arise: a gravity number, N_{Gr},

$$N_{\text{Gr}} = \frac{\rho g L}{\gamma / \sqrt{k}}, \tag{12}$$

and a group associated with the higher-order term, or macroscopic surface tension, N_Γ,

$$N_\Gamma = \frac{\Gamma}{\rho g L^3}. \tag{13}$$

In [24], we argue that the macroscopic surface tension arises from phenomena that are already represented in the basic model parameters. Thus, we relate the characteristic length scale of this phenomenon to the length scales already present in the problem. In particular, we propose that the relevant length scale is the capillary rise. Under this choice, since $\Gamma/\rho g$ has units of length cube, we take $\Gamma \sim h_{\text{cap}}^3$, where the Leverett scaling [58] suggests

$$h_{\text{cap}} \sim \frac{\gamma}{\rho g \sqrt{k}}. \tag{14}$$

This implies the relationship

$$N_\Gamma \sim N_{\text{Gr}}^{-3}, \tag{15}$$

and the dimensionless model equation reads

$$\frac{\partial S}{\partial t} + \nabla \cdot \left[k_r(S) \nabla \left(z + N_{\text{Gr}}^{-1} J(S) + N_{\text{Gr}}^{-3} \nabla^2 S \right) \right] = 0. \tag{16}$$

In heterogeneous media we define the space-dependent permeability field as $k(\boldsymbol{x}) = \tilde{k} k_D(\boldsymbol{x})$, where $\tilde{k}$ is the average permeability and the dimensionless permeability field $k_D(\boldsymbol{x})$ incorporates the spatial variability. Therefore, the nondimensional model equation is

$$\frac{\partial S}{\partial t} + \nabla \cdot \left[k_D(\boldsymbol{x}) k_r(S) \nabla \left(z + N_{\text{Gr}}^{-1} J(S) + N_{\text{Gr}}^{-3} \nabla^2 S \right) \right] = 0. \tag{17}$$

The above expression assumes that heterogeneity affects the mobility, but not the capillary pressure.

2.2. Strong form of the mathematical problem

Let the problem be defined on a domain Ω, which is an open subset of $\mathbb{R}^3$. The boundary of Ω, assumed sufficiently smooth, is called $\partial\Omega$. We assume that $\partial\Omega$ is composed of two complementary parts $\partial\Omega = \overline{\partial\Omega_D \cup \partial\Omega_N}$. The unit outward normal to $\partial\Omega$ is denoted $\boldsymbol{n}$. We denote a generic point of Ω by $\boldsymbol{x}$. In strong and dimensionless form, the problem can be stated as: find the water saturation $S : \overline{\Omega} \times [0, T] \mapsto [0, 1]$ such

that

$$\frac{\partial S}{\partial t} + \nabla \cdot \left(k_D(\boldsymbol{x}) k_r(S) \nabla \left(z + N_{\mathrm{Gr}}^{-1} J(S) + N_{\mathrm{Gr}}^{-3} \nabla^2 S \right) \right) = 0 \qquad \text{in} \quad \Omega \times (0,T), \tag{18.1}$$

$$S(\boldsymbol{x},t) = S_{\mathrm{in}}(\boldsymbol{x},t) \qquad \text{on} \quad \partial\Omega_D \times [0,T], \tag{18.2}$$

$$\nabla \left(z + N_{\mathrm{Gr}}^{-1} J(S) + N_{\mathrm{Gr}}^{-3} \nabla^2 S \right) \cdot \boldsymbol{n} = 0 \qquad \text{on} \quad \partial\Omega_N \times [0,T], \tag{18.3}$$

$$\nabla S \cdot \boldsymbol{n} = 0 \qquad \text{on} \quad \partial\Omega \times [0,T], \tag{18.4}$$

$$S(\boldsymbol{x},0) = S_0(\boldsymbol{x}) \qquad \text{in} \quad \overline{\Omega}. \tag{18.5}$$

where t denotes the time, $[0,T]$ is the time interval, and $S_{\mathrm{in}} : \partial\Omega_D \times [0,T] \mapsto \mathbb{R}$, $S_0 : \overline{\Omega} \mapsto \mathbb{R}$ are given functions that define, respectively, the boundary and initial conditions. The rest of the notation is as follows: z is the spatial direction (i.e., a cartesian component of $\boldsymbol{x}$) that points downwards, in the direction of gravity, N_{Gr} is a positive dimensionless number that sets the intrinsic length scale of the problem, and $k_D : \overline{\Omega} \mapsto \mathbb{R}^+$ is the dimensionless permeability field. The nonlinear functions of saturation $k_r : [0,1] \mapsto \mathbb{R}^+$ and $J : [0,1] \mapsto \mathbb{R}$ represent the relative permeability and dimensionless capillary pressure functions, respectively. Here, we follow [25] and employ

$$k_r(S) = S^m, \tag{19.1}$$

$$J(S) = S^{-1/\lambda} \left[1 - e^{-\kappa(1-S)} \left(1 + \kappa \frac{\lambda}{\lambda - 1} S \right) \right]. \tag{19.2}$$

In equations (19.1)–(19.2) m, λ and κ are positive constants that define the soil properties. Equation (19.1) is widely utilized for homogeneous sands, and the parameter m normally ranges from 4 to 10 depending on the soil characteristics. Equation (19.2) is an extension of the Brooks-Corey capillary pressure function [13], in which κ is a compressibility parameter that may be thought of as a large penalty constant that energetically penalizes the fully saturated state. In this paper, we take $\kappa = 50$, and $\lambda = 4$. These are physically relevant values, that lead to quantitative agreement with laboratory experiments [25].

3. Numerical formulation

Here we describe our numerical formulation for the infiltration theory presented in the previous section. From the point of view of space discretization, the numerical simulation of equation (18.1) is challenging for two reasons. First, the equation develops sharp internal layers that travel through the computational domain. Those layers have complex topology, typically exhibiting a small undershoot and a large overshoot within the characteristic length of the layer, which, in turn, is very small compared to the macroscopic scale of the problem. The second reason why the numerical discretization of this equation is challenging is the presence of higher-order partial-differential operators. Here, we employ a numerical formulation based on Isogeometric Analysis, a technology recently introduced in the field of computational mechanics that permits generating conforming discretizations for higher-order operators in a straightforward manner [20, 51].

3.1. Continuous problem in variational form

We begin by considering a weak form of equation (18.1). Let $\mathscr{S}$ and $\mathscr{W}$ denote the trial solution and weighting functions spaces, respectively. The computational domain is the box $\Omega = (0,L)^3$ parameterized

by cartesian coordinates (x, y, z), where z points downwards in the direction of gravity. In the direction of gravity we impose a given water flux on the top of the domain ($\partial\Omega_D$), and outflow boundary conditions on the bottom of the domain ($\partial\Omega_N$). On the lateral boundaries of the box we will impose periodic boundary conditions in the x and y directions (note that this represents a slight variation with respect to the boundary value problem posed in (18), but still defines a well-posed problem). On $\partial\Omega_D$, we impose $S = S_{\text{in}}$ and $\nabla S \cdot \boldsymbol{n} = 0$, which is asymptotically equivalent to imposing a flux ratio (dimensionless infiltration rate), R_s, given by $R_s = k_r(S_{\text{in}})$. These restrictions are imposed strongly on the finite element spaces. On $\partial\Omega_N$, we impose outflow boundary conditions, given by (18.3) and (18.4). The first condition, (18.3), is naturally imposed by the variational formulation, while the second, (18.4), is strongly enforced on the finite element spaces. Thus, the functional spaces $\mathscr{S}$ and $\mathscr{W}$ can be defined as follows,

$$\mathscr{S} = \left\{ S \in \mathcal{H}^2 \,|\, S = S_{\text{in}} \text{ on } \partial\Omega_D,\, \nabla S \cdot \boldsymbol{n} = 0 \text{ on } \overline{\partial\Omega_D \cup \partial\Omega_N},\, S \text{ periodic in } x \text{ and } y \text{ directions} \right\} \tag{20}$$

$$\mathscr{W} = \left\{ W \in \mathcal{H}^2 \,|\, W = 0 \text{ on } \partial\Omega_D,\, \nabla W \cdot \boldsymbol{n} = 0 \text{ on } \overline{\partial\Omega_D \cup \partial\Omega_N},\, W \text{ periodic in } x \text{ and } y \text{ directions} \right\} \tag{21}$$

where $\mathcal{H}^2$ is the Sobolev space of square integrable functions with square integrable first and second derivatives. Therefore, the variational formulation can be stated as follows: find $S \in \mathscr{S}$ such that $\forall W \in \mathscr{W}$,

$$\mathsf{B}(W, S) = 0, \tag{22}$$

where

$$\mathsf{B}(W,S) = \int_\Omega W \frac{\partial S}{\partial t} \mathrm{d}\Omega - \int_\Omega \nabla W \cdot k_D(\boldsymbol{x}) k_r(S) \nabla(z + N_{\text{Gr}}^{-1} J(S)) \mathrm{d}\Omega + \int_\Omega \nabla \cdot (k_D(\boldsymbol{x}) k_r(S) \nabla W) N_{\text{Gr}}^{-3} \nabla^2 S \mathrm{d}\Omega \tag{23}$$

Note that $\mathscr{S}$ and $\mathscr{W}$ need to be subsets of $\mathcal{H}^2$, otherwise we would be unable to make sense out of the last integral in (23).

3.2. The semidiscrete formulation

For the space discretization of (22) we define finite-dimensional trial and weighting function spaces, denoted by $\mathscr{S}^h$ and $\mathscr{W}^h$, respectively. We employ a conforming discretization, which implies that the conditions $\mathscr{S}^h \subset \mathscr{S}$ and $\mathscr{W}^h \subset \mathscr{W}$ are satisfied. We use the Galerkin method, so a member of $\mathscr{S}^h$ is constructed by taking a member of $\mathscr{W}^h$ and adding a sufficiently smooth function that verifies the essential boundary conditions. The variational problem over the finite-dimensional spaces may be stated as follows: find $S^h \in \mathscr{S}^h$ such that $\forall W^h \in \mathscr{W}^h$

$$\mathsf{B}(W^h, S^h) = 0, \tag{24}$$

where W^h is defined as

$$W^h = \sum_{A=1}^{n_b} W_A N_A. \tag{25}$$

The N_A's are the basis functions, and n_b is the dimension of the discrete space. Note that the condition $\mathscr{W}^h \subset \mathscr{W}$ mandates our discrete space to be at least $\mathcal{H}^2$-conforming [12]. In what follows, we show how to construct $\mathcal{H}^2$-conforming NURBS discrete spaces.

3.3. Discrete space

In the spirit of the finite element method, the basis functions are generated on a parametric space, and then mapped onto the physical space using a geometrical mapping. For the geometries considered in this work, NURBS reduce to B-Splines. Thus, we show how to generate a B-Spline basis on the parametric space. We start our presentation with a one-dimensional B-Spline basis, which is a set of n piecewise polynomial functions of order p denoted by $\{B_{i,p}\}_{i=1,\dots,n}$. These functions are generated from a knot vector, which is a set of non-decreasing coordinates in parametric space called knots. Let us introduce the following knot vector

$$\boldsymbol{K}_\xi = \{\xi_1, \xi_2, \dots, \xi_{n+p+1}\}. \tag{26}$$

Without loss of generality, it may be assumed that $\xi_1 = 0$ and $\xi_{n+p+1} = 1$, and the basis functions are defined on the interval $[0, 1]$, which we associate to the parametric space. Given p and $\boldsymbol{K}_\xi$, we define the zeroth-order B-Spline functions $\{B_{i,0}\}_{i=1,\dots,n}$ as

$$B_{i,0}(\xi) = \begin{cases} 1 & \text{if} \quad \xi_i \le \xi \le \xi_{i+1}, \\ 0 & \text{otherwise.} \end{cases} \tag{27}$$

The p-th order B-Splines basis functions are defined recursively using the relation

$$B_{i,q}(\xi) = \frac{\xi - \xi_i}{\xi_{i+p} - \xi_i} B_{i,q-1}(\xi) + \frac{\xi_{i+p+1} - \xi}{\xi_{i+p+1} - \xi_{i+1}} B_{i+1,q-1}(\xi); \quad i = 1, \dots, n; \quad q = 1, \dots, p. \tag{28}$$

The functions $\{B_{i,p}\}_{i=1,\dots,n}$ are $\mathcal{C}^\infty$ everywhere except at the knots. At a non-repeated knot, the functions have $p-1$ continuous derivatives. If a knot is repeated k times the number of continuous derivatives at that point is $p - 1 - k$.

To generate a three-dimensional B-Spline basis, we need three polynomial orders p^α, $\alpha = 1, 2, 3$ and three knot vectors $\boldsymbol{K}_\gamma$, $\gamma = \xi^1, \xi^2, \xi^3$ of lengths $n^\alpha + p^\alpha + 1$, respectively. Three-dimensional B-Spline functions are defined by taking tensor products of their one-dimensional counterparts as follows:

$$B_{\boldsymbol{i}}(\xi^1, \xi^2, \xi^3) = \otimes_{\gamma=1}^{3} B_{i^\gamma, p^\gamma}(\xi^\gamma), \tag{29}$$

where $\boldsymbol{i} = \{i^1, i^2, i^3\}$. We denote Ξ the parametric space, which may be assumed to be $\Xi = [0, 1]^3$. Using the functions (29) we can generate a volumetric object $V = \boldsymbol{F}(\boldsymbol{\xi})$ by way of the geometrical map $\boldsymbol{F}$ such that

$$\boldsymbol{F}(\boldsymbol{\xi}) = \sum_{i \in I} \boldsymbol{C}_{\boldsymbol{i}} B_{\boldsymbol{i}}(\boldsymbol{\xi}) \quad \forall \boldsymbol{\xi} \in \Xi, \tag{30}$$

where $\boldsymbol{C}_{\boldsymbol{i}} \in \mathbb{R}^3$ are the control points and $I = \left\{ \boldsymbol{i} = \{i^1, i^2, i^3\} \in \mathbb{N}^3,\ i^k = 1, \dots, n^k + p^k + 1 \right\}$.

B-Spline functions in physical space are defined as the push forward of the functions $B_{\boldsymbol{i}}$, $\boldsymbol{i} \in I$. The discrete space that we use for our numerical method is the space spanned by those functions, namely

$$\mathcal{V}^h = \text{span}\{B_{\boldsymbol{i}} \circ \boldsymbol{F}^{-1},\ \boldsymbol{i} \in I\}. \tag{31}$$

Note that we invoke the isoparametric concept, because the geometrical mapping $\boldsymbol{F}$ is defined in terms of B-Spline functions.

3.4. Time discretization

Time integration of the proposed infiltration equation is demanding because of the nonlinear fourth-order term in equation (18.1). Probably, the most common approach for equations of this type is the use of first-order accurate semi-implicit schemes. These methods are widely used for fourth-order partial differential equations in which the fourth-order term is linear. In that case, the higher-order term is treated implicitly, while the nonlinear lower-order terms are treated explicitly. This scheme renders a linearly implicit algorithm which avoids the use of a nonlinear solver, and permits taking somewhat larger time steps than a fully explicit method. This idea has been used extensively [47]. When the fourth-order term is nonlinear, this procedure needs to be modified to obtain a linearly implicit method. Zhu et al. [82] proposed a linearly implicit first-order accurate algorithm that permits taking somewhat larger time steps than Euler's method. However, as shown in [44], first-order accurate algorithms normally lead to excessive numerical dissipation that may even suppress an instability built into the physics of the equations. For these reasons, we favor the use of fully-implicit second-order accurate algorithms. In this work, we employ the generalized-α [19, 53] method, which is a second-order accurate A-stable method with optimal high-frequency dissipation. In what follows, we present our implementation of the generalized-α method. Let us divide the time interval $[0, T]$ into N subintervals $I_n = [t_n, t_{n+1}),\ n = 1, \ldots, N$ with $0 < t_0 < t_1 < \cdots < t_N = T$. We define the time step size at stage n as $\Delta t_n = t_{n+1} - t_n$. Let us define the global vector of degrees of freedom

$$\boldsymbol{S}_n = \{S_{n,B}\}_{B=1,\ldots,n_b}. \tag{32}$$

The vector $\boldsymbol{S}_n$ contains the coordinates on $\mathscr{S}^h$ of the trial function S^h_n, which is the time discrete counterpart of $S^h(\cdot, t_n)$. The generalized-α method also involves another global vector $\dot{\boldsymbol{S}}_n$ which allocates the coordinates of the discrete approximation to $\frac{\partial S^h}{\partial t}(\cdot, t_n)$. These two global vectors are treated independently, but they are related to each other through the linear relationship

$$\boldsymbol{S}_{n+1} = \boldsymbol{S}_n + \Delta t_n \dot{\boldsymbol{S}}_n + \gamma \Delta t_n (\dot{\boldsymbol{S}}_{n+1} - \dot{\boldsymbol{S}}_n), \tag{33}$$

where γ is a parameter of the algorithm. Let us define the following residual vector

$$\boldsymbol{R} = \{R_A\}_{A=1,\ldots,n_b} \quad \text{where} \quad R_A = B(N_A, S^h). \tag{34}$$

This residual vector is at each time step equated to zero, collocating the saturation and saturation time derivative at times $t_{n+\alpha_f}$ and $t_{n+\alpha_m}$, respectively. Thus, the fundamental equations of the algorithm are

$$\boldsymbol{R}(\boldsymbol{S}_{n+\alpha_f}, \dot{\boldsymbol{S}}_{n+\alpha_m}) = 0, \tag{35}$$

$$\boldsymbol{S}_{n+\alpha_f} = \boldsymbol{S}_n + \alpha_f (\boldsymbol{S}_{n+1} - \boldsymbol{S}_n), \tag{36}$$

$$\dot{\boldsymbol{S}}_{n+\alpha_m} = \dot{\boldsymbol{S}}_n + \alpha_m (\dot{\boldsymbol{S}}_{n+1} - \dot{\boldsymbol{S}}_n), \tag{37}$$

$$\boldsymbol{S}_{n+1} = \boldsymbol{S}_n + \Delta t_n \dot{\boldsymbol{S}}_n + \gamma \Delta t_n (\dot{\boldsymbol{S}}_{n+1} - \dot{\boldsymbol{S}}_n), \tag{38}$$

where α_f and α_m are real-valued parameters that control the accuracy and stability of the algorithm. One can prove that, for a linear problem, unconditional stability is achieved if

$$\alpha_m \geq \alpha_f \geq 1/2, \tag{39}$$

and second-order time accuracy is attained if

$$\gamma = \frac{1}{2} + \alpha_m - \alpha_f. \tag{40}$$

The parameters α_m and α_f may be parameterized in terms of ϱ_∞, the spectral radius of the amplification matrix for an infinite time step, as follows,

$$\alpha_m = \frac{1}{2}\left(\frac{3-\varrho_\infty}{1+\varrho_\infty}\right); \quad \alpha_f = \frac{1}{1+\varrho_\infty}. \tag{41}$$

Taking $\varrho_\infty \in [0,1]$ in (41), α_m and α_f satisfy automatically the A-stability condition (39), and we only need to set γ according to (40) to define a second-order accurate method. It is known that ϱ_∞ controls high-frequency dissipation, so we can have control over this property of the algorithm. For example, if we take $\varrho_\infty = 1$, the method becomes the midpoint rule, which is known to preserve all frequencies for a linear problem. If we take $\varrho_\infty = 0$, the algorithm applied to a linear problem annihilates the highest frequency in one step. We found that $\varrho_\infty = 0.5$ provides a good balance between accuracy and dissipation in the simulations. Such value of the ϱ_∞ parameter is commonly used in other applications of the generalized-α algorithm (see, e.g., [6]).

We implement the generalized-α algorithm as follows: given $\boldsymbol{S}_n$ and $\dot{\boldsymbol{S}}_n$, we employ the following predictions for $\boldsymbol{S}_{n+1}$ and $\dot{\boldsymbol{S}}_{n+1}$

$$\boldsymbol{S}_{n+1}^{(0)} = \boldsymbol{S}_n^{(0)}, \tag{42}$$

$$\dot{\boldsymbol{S}}_{n+1}^{(0)} = \frac{\gamma-1}{\gamma}\dot{\boldsymbol{S}}_n. \tag{43}$$

Note that $\boldsymbol{S}_{n+1}^{(0)}$ is just the zeroth-order approximation for the saturation and $\dot{\boldsymbol{S}}_{n+1}^{(0)}$ is the consistent prediction for $\dot{\boldsymbol{S}}_{n+1}$ that follows from equation (38). We employ these predictions to start a Newton-based iterative process to solve the nonlinear system of algebraic equations (35). Thus, for $i = 0$ to $i = i_{\max}$, given $\boldsymbol{S}_{n+1}^{(i)}$ and $\dot{\boldsymbol{S}}_{n+1}^{(i)}$, we compute $\boldsymbol{S}_{n+1}^{(i+1)}$ and $\dot{\boldsymbol{S}}_{n+1}^{(i+1)}$ as follows:

(1) We use the i-th iterates $\boldsymbol{S}_{n+1}^{(i)}$ and $\dot{\boldsymbol{S}}_{n+1}^{(i)}$ to assemble the residual vector

$$\boldsymbol{R}^{(i)} = \boldsymbol{R}(\boldsymbol{S}_{n+\alpha_f}^{(i)}, \dot{\boldsymbol{S}}_{n+\alpha_m}^{(i)}), \tag{44}$$

and the tangent matrix $\boldsymbol{K}^{(i)} = \{K_{AB}^{(i)}\}_{A,B=1,\ldots,n_b}$. Since $\boldsymbol{S}$ and $\dot{\boldsymbol{S}}$ are indeed related through equation (38), we may use increments of $\boldsymbol{S}$ or $\dot{\boldsymbol{S}}$ to advance Newton's algorithm. In this work, we use increments of $\dot{\boldsymbol{S}}$, which leads to the tangent matrix

$$K_{AB}^{(i)} = \frac{\partial R_A^{(i)}}{\partial \dot{S}_{n+1,B}^{(i)}}. \tag{45}$$

An explicit expression for $K_{AB}^{(i)}$ may be obtained using the chain rule and the relation (38) into equation (45). This leads to

$$K_{AB}^{i} = \frac{\partial R_A^{(i)}}{\partial S_{n+\alpha_f,B}^{(i)}}\frac{\partial \boldsymbol{S}_{n+\alpha_f,B}^{(i)}}{\partial \dot{\boldsymbol{S}}_{n+1,B}^{(i)}} + \frac{\partial R_A^{(i)}}{\partial \dot{\boldsymbol{S}}_{n+\alpha_m,B}^{(i)}}\frac{\partial \dot{\boldsymbol{S}}_{n+\alpha_m,B}^{(i)}}{\partial \dot{\boldsymbol{S}}_{n+1,B}^{(i)}} = \alpha_f\gamma\Delta t_n\frac{\partial \boldsymbol{S}_{n+\alpha_f,B}^{(i)}}{\partial \dot{\boldsymbol{S}}_{n+1,B}^{(i)}} + \alpha_m\frac{\partial \dot{\boldsymbol{S}}_{n+\alpha_m,B}^{(i)}}{\partial \dot{\boldsymbol{S}}_{n+1,B}^{(i)}}. \tag{46}$$

(2) Solve the linear system

$$\boldsymbol{K}^{(i)}\Delta\dot{\boldsymbol{S}}_{n+1}^{(i)} = -\boldsymbol{R}^{(i)} \tag{47}$$

to a given tolerance using the GMRES algortihm [70].

(3) Update the solution as

$$\dot{\boldsymbol{S}}_{n+1}^{(i+1)} = \dot{\boldsymbol{S}}_{n+1}^{(i)} + \Delta\dot{\boldsymbol{S}}_{n+1}^{(i)}, \tag{48}$$

$$\boldsymbol{S}_{n+1}^{(i+1)} = \boldsymbol{S}_{n+1}^{(i)} + \gamma\Delta t_n\Delta\dot{\boldsymbol{S}}_{n+1}^{(i)}. \tag{49}$$

Steps (1)-(3) complete a nonlinear iteration. This process needs to be repeated until the value of the residual has been reduced to a given tolerance ε of its initial value in a given time step. We used the value $\varepsilon = 10^{-5}$ in all our numerical simulations.

3.5. Time step adaptivity

Homogeneous soils give rise to fingers that infiltrate with an approximately constant velocity, and, thus, taking a fixed time step throughout the simulation is an adequate strategy. Highly heterogeneous soils lead to significant variations in finger velocities, which affects the time integration of the semidiscrete equations. We found that for highly heterogeneous soils it is important to use adaptive time stepping. There are several options to dynamically adapt the time step in the generalized-α method, but we follow the strategy proposed in [43]. This method is based on the fact that the generalized-α algorithm becomes the backward Euler method when $\alpha_m = \alpha_f = \gamma = 1$. Thus, we compute every time step twice; first, we use the backward Euler method, and then we use generalized-α with $\varrho_\infty = 0.5$. We use the obtained results to compute the $\mathcal{L}^2$ norm of the normalized difference of both saturation fields, which we call e. This quantity may be thought as an error estimate for the backward Euler method. The value of e is compared with a threshold error, $\tau = 10^{-3}$. If e is greater than τ or Newton's method did not converge for any of the time integration schemes, we repeat the time step using $\widetilde{\Delta t_n} = s\Delta t_n$, where $s = 0.9$ and n is the current time step. If e is lower than τ, we advance to the next time step and update the time-step size using the formula

$$\Delta t_{n+1} = s\sqrt{\frac{\tau}{e}}\,\Delta t_n. \tag{50}$$

4. Numerical examples

Here, we study unstable infiltration, that is, the process in which water infiltrates a previously dry porous medium through preferential vertical paths (we refer to these preferential paths as "fingers"). We call stable infiltration the process in which water infiltrates the medium as a flat horizontal front. The infiltration of water may be stable or unstable depending upon several factors, such as, for example, the infiltration rate or the soil characteristics. Stability, in this context, refers to whether the infiltration is stable or unstable in terms of the control parameters, primarily the infiltration rate.

Our simulations explore several aspects of the spatial and temporal discretization of partial differential equations with higher-order terms, in the context of pattern formation during gravity-driven infiltration. In section 4.1, we analyze the convergence of the finger patterns under h-refinement, focusing on the challenge of

accurate discretization of these models. In the sections that follow (4.2–4.4), we explain the dynamics of the governing equations and provide insights into the physics of the problem. In section 4.2, we present a series of two-dimensional simulations with increasing infiltration fluxes, illustrating the onset and suppression of the fingering instability, as well as the length scale of the finger patterns. An essential feature of flow through real field soils is the presence of spatial heterogeneity in the permeability field; in section 4.3, we study the implications of heterogeneous and anisotropic conductivity fields, and frame the discussion in the context of the relative dominance of instability and soil structure with respect to flow. Finally, in section 4.4, we present three-dimensional simulations of gravity fingering. These are the first 3D simulations of this phenomenon to date.

For all the numerical examples we impose inflow boundary conditions (equations (18.2) and (18.4)) on $\partial\Omega_D$ (top of the domain), outflow boundary conditions (equations (18.3) and (18.4)) on $\partial\Omega_N$, and periodicity on the lateral boundaries.

4.1. Accuracy study

Our model equation is strongly nonlinear, and planar wetting fronts are unstable for a wide range of physical parameters and infiltration rates. Therefore, it is difficult to rigorously quantify the convergence of the spatial and temporal discretization. In this section, we qualitatively assess the convergence and efficiency of the proposed discretization. We solve a typical infiltration example and observe how the saturation field converges under grid refinement (Figure 1). The flow is initialized assuming a perturbed flat wetting front near the top of the domain with saturation S_{in}. The initial saturation of the soil, $S_0 = 0.01$ is imposed elsewhere in the domain. The transition between the two values of the saturation (S_{in} and S_0) is not discontinuous, but is modeled with a hyperbolic tangent function. We set the exponent of the relative permeability curve to $m = 4$ and evolve the saturation field using a series of grids with increasing levels of spatial refinement. All the grids are uniform, and we consider resolutions of 256^2, 512^2, and 1024^2 $\mathcal{C}^1$ quadratic elements. The solution is advanced in time using a constant time step $\Delta t = 0.25$.

Figure 1 shows the numerical approximation of the saturation field at time $t = 147.5$, computed using the three grids. At the scale of the plot, we do not observe significant differences between the results on different meshes, but the discrepancies become more apparent when we represent horizontal and vertical cutlines of the saturation field. The cutlines are taken at the locations indicated in Figures 1(a)–1(c), and are depicted in Figures 1(d)–1(e). The saturation overshoot at the finger tips is significantly underestimated on the coarser meshes (Figure 1). This fact has physical significance because the wetting front stability is strongly correlated with the presence of saturation overshoot [24, 29, 33, 38]. In fact, it has been shown from a linear stability analysis of the continuum theory that the strength of the instability, measured by the growth factor of the most unstable mode, is directly related to the magnitude of the saturation overshoot [25]. Figure 1(e) shows the typical profile of a gravity-driven finger. The profile exhibits a rather large overshoot, and a very small undershoot (see the inset in Figure 1(e)) across the interface layer. These small features of the solution play a role in the dynamics of the flow, and need to be resolved by the computational mesh to ensure accuracy of the numerical solution. As future work, we envision the use of local refinement procedures that retain the conforming nature of the discretization. The use of T-Splines [5] or hierarchical B-Splines

[71] seem to be promising possibilities.

This example illustrates the complexity of the numerical simulations of the phase-field infiltration theory. Fully resolving the wetting front requires using fine spatial meshes, especially for high values of the relative permeability exponent m (for homogeneous sandy soils, m may be as high as 10 [25, 29]). By taking different values for m, we explore the effect of this constitutive parameter on the physics of the problem and on the numerics. Higher values of m lead to a stronger fingering instability, which require a finer computational mesh. In the next examples, especially on those performed in three-dimensional domains, we are unable to fully resolve the wetting front, just as we are unable to solve all the relevant length scales in a turbulent fluid flow. However, we feel that our simulations reproduce the fundamental features of unstable fluid flow into a porous medium. In fact, one of the noteworthy features of our computational method is its ability to solve the equations for high values of m using relatively coarse meshes.

4.2. Onset and suppression of the instability: finger length scales

One of the important factors in the numerical simulation of unstable infiltration is that the finger length scales depend strongly on the imposed infiltration flux, rather than just on model parameters and constitutive relations (see Figure 2, where the only differences between the images are the infiltration rates and the computational times). For the calculations in this section, the computational domain is $\Omega = (0, 2)^2$, and we take $N_{\mathrm{Gr}} = 50$, $\kappa = 50$, and $\lambda = 4$ in equation (19.2). For the relative permeability we set $m = 7$. The hydraulic conductivity is mildly heterogeneous, with isotropic, multi-Gaussian statistics with an exponential semivariogram model, and correlation lengths $l_x = l_y = 4h$, where $h = 1/256$ is the mesh size. The permeability field is generated using the method proposed in [39]. The initial condition is the same as in section 4.1. We specified different infiltration fluxes by varying the imposed saturation at the upper boundary. For low infiltration rates, the water infiltrates the soil through multiple thin fingers, with low saturation. The separation between fingers is typically larger than the characteristic finger size. As the infiltration flux increases, the fingers become thicker, and the separation between fingers decreases, being similar to the finger size. For high infiltration rates of the order of the saturated conductivity, $S_{\mathrm{in}} \approx 1$, the wetting front is stable, and water imbibes the soil compactly, as a quasi-1D process. The stability diagram emerging from our simulations is consistent with experimental observations [42], because stable infiltration (i.e., a flat wetting front) is predicted for high infiltration rates, while unstable infiltration (i.e., a fingered wetting front) is encountered for intermediate infiltration rates. From a computational perspective, the demands on the accuracy and robustness of the discretization change with the flow pattern. For low infiltration rates, the characteristic length scale of the flow features is smaller, but the fronts are somewhat smoother. On the other hand, for high infiltration fluxes the flow is quasi-1D, but the wetting front is extremely sharp.

4.3. Effect of heterogeneous permeability: robustness of the numerical scheme

In this section we analyze the impact of the medium heterogeneity on the robustness of the discretization. Field soils may exhibit strong heterogeneity or structure, that is, a conductivity field with strong spatial variations. These variations exhibit characteristic correlations in space. For simplicity, here we consider heterogeneity in the saturated hydraulic conductivity only, therefore neglecting the influence of heterogeneity

on the capillary terms. We also assume that the nonlinear structure of the relative permeability does not vary in space, $k_r(S) = S^5$. We construct hydraulic conductivity fields with multi-Gaussian statistics with an exponential semivariogram model, generated from a lognormal distribution of permeabilities defined by the variance, $\sigma^2_{\ln k}$, and correlation lengths in x and y directions, denoted by l_x and l_y, respectively. For more details about the permeability fields the reader is referred to [39]. The basic setup for these calculations is the same as in the previous examples. In this case we take $S_{\text{in}} = 0.2$ and $S_0 = 0.01$.

We control the strength of the heterogeneity by the variance of the log-permeability field. We model layered soil structures by introducing anisotropy in the correlation lengths, i.e., by setting $l_x \neq l_y$. Numerically, we analyze the interaction between the heterogeneity variance and correlation lengths and the finger dynamics.

4.3.1. Isotropic permeability fields

For isotropically-correlated permeability fields we focus on the interaction between the characteristic finger size and the correlation length, $l_x = l_y \equiv l$, of the heterogeneity. We consider two values of the variance of the dimensionless log-conductivity, $\sigma^2_{\ln k} = 1$ (Figure 3) , and $\sigma^2_{\ln k} = 4$ (Figure 4). In both cases, we study permeability fields with increasing correlation lengths $l = h$, $l = 4h$, and $l = 8h$, where h is the mesh size. Note that for $\sigma^2_{\ln k} = 4$ the saturated conductivity varies over roughly five orders of magnitude. Qualitatively, heterogeneity induces meandering of the fingers, which also exhibit a non-homogeneous distribution of water content within the fingers. When the correlation length of the permeability field is much smaller than the typical finger size, the heterogeneity induces a slight meandering of the fingers, without significantly changing the overall flow pattern. As the correlation length approaches the finger size, the meandering is exacerbated, inducing recombination and merging of the fingers. For correlation lengths that are larger than the finger size, the dynamics of the fingers recover their strong vertical nature, but the finger separation changes drastically.

We also employ these simulations to study the effect of heterogeneity on the infiltration time scales. We analyze the time evolution of the time step selected by our adaptive algorithm (Figure 5). The time intervals in the plots range from time zero to the time at which the fingers reach the bottom of the domain. Figure 5(a) shows that when the correlation length of the permeability field is much smaller than the typical finger size, changing the variance of the heterogeneity does not modify significantly the infiltration time scales. The average finger velocity is very similar for $\sigma^2_{\ln k} = 1$ and $\sigma^2_{\ln k} = 4$, just as the average time step employed by our algorithm. As the correlation length approaches the finger size, the situation changes significantly. The infiltration is much faster for $\sigma^2_{\ln k} = 4$ than for $\sigma^2_{\ln k} = 1$. The reason is that for this correlation length, the fingers can deviate from their natural vertical pattern to find high-permeability paths. This phenomenon leads to a much more effective infiltration for $\sigma^2_{\ln k} = 4$. We also note that the average time step taken by our adaptive algorithm is about an order of magnitude smaller for $\sigma^2_{\ln k} = 4$, suggesting faster dynamics, and indicating that our adaptive strategy adequately captures the relevant infiltration time scales. The variance of the permeability field makes an even more significant difference for larger correlation lengths. We observe in Figure 5(c) that for $\sigma^2_{\ln k} = 4$, the infiltration is about one order of magnitude faster than for $\sigma^2_{\ln k} = 1$. The time steps are consistent with these times scales.

Finally, we note that higher variances of the permeability field lead to a wider range of relevant time

scales for the infiltration dynamics. Our adaptive time stepping algorithm captures this phenomenon. For all correlation lengths, the ratio of the maximum to the minimum time step increased by a factor of approximately 4 when we raised the variance from $\sigma^2_{\ln k} = 1$ to $\sigma^2_{\ln k} = 4$.

4.3.2. Anisotropic permeability fields

Structural layering and anisotropically-correlated permeability are often found in natural soils. By controlling the ratio between the correlation lengths l_x and l_y, we simulate the effects of layering in the soil structure. Figure 6 corresponds to $\sigma^2_{\ln k} = 1$, while Figure 7 corresponds to $\sigma^2_{\ln k} = 4$. Strongly anisotropic permeability fields have a significant impact on the saturation fields, although the overall pattern of preferential flow due to fingering remains. In that sense, our simulations demonstrate the pervasiveness of the fingering instability in infiltration. As expected, the impact of soil structure is more pronounced when the anisotropy is aligned vertically, although horizontal stratification is much more common in nature.

4.4. Verification of the three-dimensional code

Since we report herein the first three-dimensional simulations of unstable gravity-driven infiltration, we would like to address the verification of our three-dimensional code. Exact solutions to the infiltration theory (17) are not available, so we will utilize our three-dimensional code to produce one-dimensional traveling wave solutions to the model. The traveling wave solutions can be obtained to high precision using an overkill solution produced by a rational pseudospectral method with adaptively transformed Chebyshev nodes [75, 28]. To obtain the traveling waves, we seek solutions of the form

$$S(x, y, z, t) = u(\zeta) = u(z - ct) \tag{51}$$

where c is the wave velocity. We pose the problem on an infinite domain, and require the solution to remain bounded at infinity and satisfy

$$u(+\infty) = u^+, \quad u(-\infty) = u^- \tag{52}$$

Under these conditions, and assuming $k_D(\boldsymbol{x}) = 1$, the traveling wave velocity c is given by

$$c = \frac{k_r(u^-) - k_r(u^+)}{u^- - u^+} \tag{53}$$

Assuming that the derivatives of u vanish at infinity, the traveling wave solutions verify

$$-cu' + \frac{\mathrm{d}}{\mathrm{d}\zeta}\left(k_r(u) + N_{\mathrm{Gr}}^{-1} k_r(u) J'(u) u' + N_{\mathrm{Gr}}^{-3} k_r(u) u'''\right) = 0 \tag{54}$$

Integrating over the domain $(-\infty, +\infty)$, and imposing the conditions at infinity, we obtain the boundary value problem

$$\begin{gathered} -c(u - u^-) + k_r(u) - k_r(u^-) + N_{\mathrm{Gr}}^{-1} k_r(u) J'(u) u' + N_{\mathrm{Gr}}^{-3} k_r(u) u''' = 0 \\ u(-\infty) = u^-, \quad u(+\infty) = u^+, \quad u'(-\infty) = 0 \end{gathered} \tag{55}$$

Note that the traveling wave solutions may be thought of as stationary solutions on a moving frame of reference. We solve the problem (55) using a rational pseudospectral method on a sufficiently large domain, taking $u^+ = 0.425$ and $u^- = 0.01$. Then, we compare the solution to (55) with one-dimensional transient

solutions of the infiltration theory produced by our three-dimensional code. We observe that, for long times and a sufficiently fine mesh, the transient solutions evolve to traveling waves that match the solutions to the boundary value problem (55). This may be observed in Figure 8, where the solutions using both methods are indiscernible at the scale of the plot. The transient three-dimensional solution has been computed on a mesh composed of $1 \times 1 \times 1024$ $\mathcal{C}^1$-quadratic elements, and time-advanced over 80000 times steps of constant size $\Delta t = 6.25 \cdot 10^{-4}$. This shows significant robustness of our method and reliability for long-time calculations. Typically, the most challenging aspect of the resolution of traveling waves is capturing correctly the small undershoot of the solution located downstream of the wetting front (see the inset in Figure 8). We observe that even this small-scale feature of the solution is in agreement for both computations, which provides evidence for our three-dimensional code being correct.

We also note that the adaptive rational pseudospectral algorithm, which adaptively selects the interpolation points, and has been shown to vastly outperform standard Chebyshev collocation methods and higher-order finite differences [28], required a minimum step size of $h_{\min} \approx 0.005151$. This mesh renders a solutions with a relative error of at least $5 \cdot 10^{-4}$. The algorithm presented in this paper utlizes a uniform mesh with a mesh size of approximately $5.69 h_{\min}$, and renders a solution indiscernible at the scale of Figure 8, which suggests that our algorithm successfully combines quasi-spectral accuracy with generality, geometrical flexibility, and strong mathematical framework provided by the variational structure of the algorithm.

4.5. Three-dimensional simulations

Here we present the first three-dimensional simulations of fingering during infiltration (Figure 9). We analyze the influence of the infiltration rate flux on the stability of the wetting front. In that sense, these simulations are the 3D counterpart of those presented in section 4.1. Experimental observations have shown that the wetting front instability is a fully three-dimensional phenomenon, leading to a pattern of columnar preferential flow paths during gravity-driven imbibition into dry media [40]. Our simulations are consistent with the experiments in that the wetting front is stable for low and high infiltration rates, while it is unstable for intermediate infiltration rates. We compute our solutions in the domain $\Omega = (0, 2)^3$, with a computational mesh composed of 128^3 $\mathcal{C}^1$ uniform quadratic elements. We set the gravity number to $N_{\mathrm{Gr}} = 14$. In reference [26], the stability of the wetting front is analyzed utilizing a one-dimensional linear stability analysis that considers both modal and nonmodal effects [77]. This analysis elucidates the role of the initial water saturation and flux ratio in the stability of the system. In this section, we study the stability of the wetting front by way of large-scale numerical simulations. Our simulations confirm the results predicted in [26], which showed a transition from stable to unstable wetting fronts when the infiltration rate varies from low to intermediate values, but also demonstrate that the instability is again suppressed for large values of the flux ratio. This result is coherent with the physics of the problem and with laboratory experiments [40]. For this study we take

$$k_r(S) = \frac{1}{2}\left[S^3\left(1 + \tanh(10S - 3)\right) + S^7\left(1 - \tanh(10S - 3)\right)\right], \tag{56}$$

which is a smooth blending of the functions S^3 and S^7. This choice of the relative permeability is physically motivated [25], and allows us to work with rather coarse meshes. The main conclusion of this study would

remain the same taking standard power-law relationships. For all the numerical examples that we present in this section the initial condition is defined by a perturbed flat wetting front at a distance of 0.1 from the top boundary. The saturation takes the value S_{in} on the top of the domain and $S_0 = 0.01$ elsewhere. We present twelve simulations corresponding to twelve values of S_{in}, as shown in Figure 9. Each snapshot shows isosurfaces of water saturation when the wetting front reaches the bottom of the domain. We do not present the results at the same times because we are interested in the stability of the wetting front which is best observed when the water front reaches the bottom of the domain. Figure 9 clearly shows two transitions in the stability of the wetting front: First, the wetting front becomes unstable when we increase the flux ratio (i.e., S_{in}), as shown in the first row of the figure. Second, the wetting front shifts from unstable to stable when we increase further the flux ratio, as shown in the last row of the figure. The second and third rows show that the morphology of the fingers depends on the infiltration rate. Thin fingers are typical for low flux ratios, while higher infiltration rates lead to thicker fingers.

Additional insight may be obtained by examining slices of the solution across horizontal and vertical planes (Figure 10). The snapshots in Figure 10 illustrate typical distributions of fingers during an infiltration event, and may be employed for qualitative comparison with experiments [e.g. 40]. Finally, we present in Figure 11 the time evolution of the free-energy functional defined in Equation (3). The free-energy functional is time-decreasing for the exact solution of the infiltration theory. Figure 11 shows that, for the space-time computational mesh considered in this example, our algorithm preserves this property of the theory.

5. Conclusions

The development of theories of multiphase flow through porous media capable of reproducing hydrodynamic instabilities like gravity fingering during infiltration seems to require the introduction of higher-order terms in the mathematical description. Numerically, the presence of higher-order terms in conservation laws poses important challenges in both the spatial and temporal discretization of the equations. In this paper, we have presented a numerical algorithm for a phase-field theory of unsaturated porous media flow. The numerical simulation of the proposed governing equation requires fundamentally-new algorithms compared to those employed for the discretization of the classical Richards equation. In particular, a numerical method for the new theory should be able to handle evolving sharp interfaces, higher-order spatial derivatives, and stiffness in space and time. We propose an algorithm based on Isogeometric Analysis, a recently proposed computational technique. Isogeometric Analysis is ideally-suited for the discretization of the new theory because it enjoys excellent approximation capabilities, higher-order robustness, and globally smooth basis functions that permit a simple and efficient discretization of higher-order spatial derivatives. This numerical framework allows us to simulate a wide range of flow scenarios, including highly heterogeneous media and, for the first time, three-dimensional simulations of unstable infiltration. We have shown simulations of fingering during infiltration for different infiltration fluxes, degrees of soil heterogeneity and soil structure (anisotropy in the correlation length). Our three-dimensional examples constitute the first computations showing unstable water infiltration into a porous medium, and confirm that the new infiltration theory reproduces the fundamental features of the phenomenon.

6. Acknowledgements

H.G. gratefully acknowledges funding provided by *Xunta de Galicia* (grants # 09REM005118PR and #09MDS00718PR), *Ministerio de Ciencia a Innovación* (grants #DPI2009-14546-C02-01 and #DPI2010-16496) cofinanced with FEDER funds, and *Universidad de A Coruña*. R.J. gratefully acknowledges funding by the US Department under grant DE-SC0003907 (Early Career Award) and the ARCO Chair in Energy Studies.

[1] D.M. Anderson, G.B. McFadden, A.A. Wheeler, Diffuse-interface methods in fluid mechanics, *Annu. Rev. Fluid Mech.* **30** (1998) 139–165.

[2] I. Akkerman, Y. Bazilevs, V. M. Calo, T. J. R. Hughes, S. Hulshoff, The role of continuity in residual-based variational multiscale modeling of turbulence, *Computational Mechanics* **41** (2007) 371–378.

[3] J.W. Barret, J.F. Blowey, H. Garcke, Finite element approximation of the Cahn-Hilliard equation with degenerate mobility, *SIAM Journal of Numerical Analysis* **37** (1999) 286–318.

[4] Y. Bazilevs, V.M. Calo, J.A. Cottrell, T.J.R. Hughes, A. Reali, G. Scovazzi, Variational multiscale residual-based turbulence modeling for large eddy simulation of incompressible flows, *Computer Methods in Applied Mechanics and Engineering* **197** (2007) 173–201.

[5] Y. Bazilevs, V.M. Calo, J.A. Cottrell, J.A. Evans, T.J.R. Hughes, S. Lipton, M.A. Scott, T.W. Sederberg, Isogeometric Analysis using T-splines, *Computer Methods in Applied Mechanics and Engineering*, **199** (2010) 229–263.

[6] Y. Bazilevs, V.M. Calo, T.J.R. Hughes, Y. Zhang, Isogeometric fluid-structure interaction: theory, algorithms and computations, *Computational Mechanics*, **43** (2008) 3–37.

[7] Y. Bazilevs, T.J.R. Hughes, NURBS-based isogeometric analysis for the computation of flows about rotating components, *Computational Mechanics* **43** (2008) 143–150.

[8] J. Bear, *Dynamics of fluids in porous media*, Dover Publications, 1972.

[9] E.L. Bearer, J.S. Lowengrub, H.B. Frieboes, Y.L. Chuang, F. Jin, S.M. Wise, M. Ferrari, D.B. Agus, V. Cristini, Multiparameter computational modeling of tumor invasion, *Cancer Research* **69** (2009) 4493–4501.

[10] J.F. Blowey, C.M. Elliott, The Cahn-Hilliard gradient theory for phase separation with non-smooth free energy. Part II: Numerical analysis, *European Journal of Applied Mathematics* **3** (1992) 147–149.

[11] M.J. Borden, C.V. Verhoosel, M.A. Scott, T.J.R. Hughes, C.M. Landis, A phase-field description of dynamic brittle fracture, ICES Report (2011).

[12] S. C. Brenner, L. R. Scott, *The Mathematical Theory of Finite Element Methods*, Springer-Verlag, New York, 1994.

[13] R.H. Brooks, A.T. Corey, Properties of porous media affecting fluid flow, *J. Irrig. Drain. Div. Am. Soc. Civ. Eng.* **92** (1966) 61–88.

[14] A. Buffa, G. Sangalli, R. Vázquez, Isogeometric analysis in electromagnetics: B-splines approximation, *Computer Methods in Applied Mechanics and Engineering* **199** (2010) 1143–1152.

[15] J.W. Cahn, On spinodal decomposition, *Acta Met.* **9** (1961) 795–801.

[16] J.W. Cahn, J.E. Hilliard, Free energy of a non-uniform system. I. Interfacial free energy, *The Journal of Chemical Physics* **28** (1958) 258–267.

[17] J.W. Cahn, J.E. Hilliard, Free energy of a non-uniform system. III. Nucleation in a two-component incompressible fluid, *The Journal of Chemical Physics* **31** (1959) 688–699.

[18] L.Q. Chen, Phase-field models for microstructural evolution, *Ann. Rev. Mater. Res.* **32** (2002) 113–140.

[19] J. Chung, G.M. Hulbert, A time integration algorithm for structural dynamics with improved numerical dissipation: The generalized-α method, *Journal of Applied Mechanics* **60** (1993) 371–375.

[20] J.A. Cottrell, T.J.R. Hughes, Y. Bazilevs, *Isogeometric Analysis: Toward integration of CAD and FEA*, Wiley, 2009.

[21] J.A. Cottrell, T.J.R. Hughes, A. Reali, Studies of refinement and continuity in isogeometric structural analysis, *Computer Methods in Applied Mechanics and Engineering* **196** (2007) 4160–4183.

[22] J.A. Cottrell, A. Reali, Y. Bazilevs, T.J.R. Hughes, Isogeometric analysis of structural vibrations, *Computer Methods in Applied Mechanics and Engineering* **195** (2006) 5257–5296.

[23] V. Cristini, X. Li, J.S. Lowengrub, and S.M. Wise, Nonlinear Simulations of Solid Tumor Growth using a Mixture Model: Invasion and Branching, *Journal of Mathematical Biology* **58** (2009) 723–763.

[24] L. Cueto-Felgueroso, R. Juanes, Nonlocal interface dynamics and pattern formation in gravity-driven unsaturated flow through porous media, *Physical Review Letters* **101** (2008) 244504.

[25] L. Cueto-Felgueroso, R. Juanes, A phase-field model of unsaturated flow, *Water Resources Research* **45** (2009) W10409.

[26] L. Cueto-Felgueroso, R. Juanes, Stability analysis of a phase-field model of graviry-driven unsaturated flow through porous media, *Physical Review E* **79** (2009) 036301.

[27] L. Cueto-Felgueroso, J. Peraire, A time-adaptive finite volume method for the Cahn-Hilliard and Kuramoto-Sivashinsky equations, *Journal of Computational Physics* **227** (2009) 9985–10017.

[28] L. Cueto-Felgueroso, R. Juanes, Adaptive rational spectral methods for the linear stability analysis of nonlinear fourth-order problems, *Journal of Computational Physics* **228** (2009) 6536–6552.

[29] D.A. DiCarlo, Experimental measurements of saturation overshoot on infiltration, *Water Resources Research* **40** (2004) W04215.

[30] F.A.L. Dullien, *Porous media: Fluid transport and pore structure*, Academic Press, 1991.

[31] C.M. Elliott, D.A. French, F.A. Milner, A 2nd-order splitting method for the Cahn-Hilliard equation, *Numerische Mathematiek* **54** (1989) 575–590.

[32] T. Elguedj, Y. Bazilevs, V.M. Calo, T.J.R. Hughes, $\bar{B}$ and $\bar{F}$ projection methods for nearly incompressible linear and non-linear elasticity and plasticity using higher-order NURBS elements, *Computer Methods in Applied Mechanics and Engineering* **197** (2008) 2732–2762.

[33] M. Eliassi, R.J. Glass, On the continuum scale modeling of gravity-driven fingers in unsaturated porous media: The inadequacy of the Richards equation with standard monotonic constitutive relations and hysteretic equations of state, *Water Resources Research* **37** (2001) 2019–2035.

[34] J.A. Evans, Y. Bazilevs, I. Babuška, T.J.R. Hughes, n-widths, sup infs, and optimality ratios for the k-version of the isogeometric finite element method, *Computer Methods in Applied Mechanics and Engineering*, **198** (2009) 1726–1741.

[35] X. Feng, A. Prohl, Analysis of a fully discrete finite element method for phase field model and approximation of its sharp interface limits, *Mathematics of Computation* **73** (2003) 541–547.

[36] D. Furihata, A stable and conservative finite difference scheme for the Cahn-Hilliard equation, *Numer. Math.* **87** (2001) 675–699.

[37] T. Fürst, R. Vodák, M. Šír, M. Bíl, On the incompatibility of Richards' equation and finger-like infiltration in unsaturated homogeneous porous media, *Water Resources Research*, **45** (2009) W03408.

[38] S.L Geiger, D.S. Durnford, Infiltration in homogeneous sands and a mechanistic model of unstable flow, *Soil Sci. Soc. Am. J.* **64** (2000) 460–469.

[39] L.W. Gelhar and C.L. Axness, Three-dimensional stochastic analysis of macrodispersion in aquifers, *Water Resources Research* **19** (1983) 161–180.

[40] R.J. Glass, S. Cann, J. King, N. Baily, J.-Y. Parlange, T.S. Steenhuis, Wetting front instability in unsaturated porous media: a three-dimensional study in initially dry sand, *Transport in Porous Media* **5** (1990) 247–268.

[41] R.J. Glass, J.-Y. Parlange, T.S. Steenhuis, Immiscible displacement in porous media: stability analysis of three-dimensional, axisymmetric disturbances with application to gravity-driven wetting front instability, *Water Resources Research* **27** (1991) 1947–1956.

[42] R.J. Glass, J.-Y. Parlange, T.S. Steenhuis, Wetting front instability: 2. Experimental determination of relationships between system parameters and two-dimensional unstable flow field behaviour in initially dry porous media , *Water Resources Research* **25** (1989) 1195–1207.

[43] H. Gomez, V.M. Calo, Y. Bazilevs, T.J.R. Hughes, Isogeometric analysis of the Cahn-Hilliard phase-field model, *Computer Methods in Applied Mechanics and Engineering* **197** (2008) 4333–4352.

[44] H. Gomez, T.J.R. Hughes, Provably unconditionally stable, second-order time-accurate, mixed variational methods for phase-field models, *Journal of Computational Physics*, **230** (2011) 5310–5327.

[45] H. Gomez, T.J.R. Hughes, X. Nogueira, V.M. Calo, Isogeometric analysis of the isothermal Navier-Stokes-Korteweg equations, *Computer Methods in Applied Mechanics and Engineering* **199** (2010) 1828–1840.

[46] H. Gomez, J. París, Numerical simulation of asymptotic states of the damped Kuramoto-Sivashinsky equation, *Physical Review E* **83** (2011) 046702.

[47] Y. He, Y. Liu, T. Tang, On large time-stepping methods for the Cahn-Hilliard equation, *Applied Numerical Mathematics*, **57** (2007) 616–628.

[48] D. E Hill, J.-Y. Parlange, Wetting front instability in layered soils, *Soil Science Society of America Journal*, **36** (1972) 697–702.

[49] T.J.R. Hughes, *The Finite Element Method: Linear Static and Dynamic Finite Element Analysis*, Dover Publications, Mineola, NY, 2000.

[50] T.J.R Hughes, A. Reali, G. Sangalli, Duality and unified analysis of discrete approximations in structural dynamics and wave propagation: comparison of p-method finite elements with k-method NURBS, *Computer Methods in Applied Mechanics and Engineering* **197** (2008) 4104–4124.

[51] T.J.R. Hughes, J.A. Cottrell, Y. Bazilevs, Isogeometric analysis: CAD, finite elements, NURBS, exact geometry and mesh refinement, *Computer Methods in Applied Mechanics and Engineering*, **194** (2005) 4135–4195.

[52] H. E. Huppert, Flow and instability of a viscous current down a slope, *Nature* **300** (1982) 427–429.

[53] K.E. Jansen, C.H. Whiting, G.M. Hulbert, A generalized-α method for integrating the filtered Navier-Stokes equations with a stabilized finite element method, *Computer Methods in Applied Mechanics and Engineering*, **190** (1999) 305–319.

[54] J. Kim, J. Lowengrub, Phase field modeling and simulation of three-phase flows, *Interfaces and Free Boundaries* **7** (2005) 435–466.

[55] J. Kim, K. Kang, J. Lowengrub, Conservative multigrid methods for Cahn-Hilliard fluids, *Journal of Computational Physics* **193** (2004) 511–543.

[56] Y. Kuramoto, T. Tsuzuki, Persistent propagation of concentration waves in dissipative media far from thermal equilibrium, *Prog. Theor. Phys.*, **55** (1976) 356–369.

[57] H.-G. Lee, J. S. Lowengrub, J. Goodman, Modeling pinchoff and reconnection in a Hele-Shaw cell. II. Analysis and simulation in the nonlinear regime, *Physics of Fluids* **14** (2002) 514-545.

[58] M. C. Leverett, Capillary behavior of porous solids, *Trans.* AIME **142** (1941) 152–169.

[59] S. Lipton, J.A. Evans, Y. Bazilevs, T. Elguedj, T.J.R. Hughes, Robustness of isogeometric structural discretizations under severe mesh distortion, *Computer Methods in Applied Mechanics and Engineering* **199** (2010) 357–373.

[60] C. Liu, J. Shen, A phase field model for the mixture of two incompressible fluids and its approximation by a Fourier-spectral method, *Physica D*, **179** (2003) 211–228.

[61] J. Lowengrub, H.B. Frieboes, F. Jin, Y.L. Chuang, X. Li, P. Macklin, S.M. Wise, V. Cristini, Nonlinear modeling of cancer: bridging the gap between cells and tomours, *Nonlinearity* **23** (2010) 1–91.

[62] J. Lowengrub, L. Truskinovsky, Quasi-incompressible Cahn-Hilliard fluids and topological transitions, *Proc. Roy. Soc. London Ser. A* **454** (1998) 2617–2654.

[63] J.L Nieber, R.Z. Dautov, A.G. Egorov, A.Y. Sheshukov, Dynamic capillary pressure mechanism for gravity-driven flows; review and extension to very dry conditions, *Transport in Porous Media* **58** (2005) 147–152.

[64] J.T. Oden, A. Hawkins, S. Prudhomme, General diffuse-interface theories and an approach to predictive tumor growth modeling, *Mathematical Models and Methods in Applied Sciences* **20** (2010) 477–517.

[65] L. Piegl, W. Tiller, *The NURBS book*, Springer, 1996.

[66] L.A. Richards, Capillary conduction of liquids through porous mediums, *Physics* **1** (1931) 318–333.

[67] A. J. Pons, A. Karma, Helical crack-front instability in mixed-mode fracture, *Nature* **464** (2010) 85–89.

[68] I. Rodriguez-Iturbe, P. D'Odorico, A. Porporato, L. Ridolfi, On the spatial and temporal links between vegetation, climate and soil moisture, *Water Resources Research* **35** (1999) 3709–3722.

[69] D.F. Rogers, *An introduction to NURBS: With historical perspective*, Morgan Kaufmann, 2000.

[70] Y. Saad, M.H. Schultz, GMRES: A generalized minimal residual algorithm for solving nonsymmetric linear systems, *SIAM Journal of Scientific and Statistical Computing* **7** (1986) 856–869.

[71] D. Schillinger, M. Ruess, N. Zander, Y. Bazilevs, A. Düster, E. Rank, Small and large deformation analysis with the p- and the B-spline versions of the Finite Cell Method, *Computational Mechanics* (2012) Published online. DOI: 10.1007/s00466-012-0684-z

[72] G.I. Sivashinsky, Nonlinear analysis of hydrodynamic instability in laminar flames. I. Derivation of basic equations, *Acta Astron.*, **4** (1977) 1177–1206.

[73] R.H. Stogner, G.F. Carey, C^1 macroelements in adaptive finite element methods, *International Journal for Numerical Methods in Engineering* **70** (2007) 1076–1095.

[74] Z.Z. Sun, A second order accurate linearized difference scheme for the two-dimensional Cahn-Hilliard equation, *Mathematics of Computation* **64** (1995) 1463–1471.

[75] T. Tee, L. Trefethen, A Rational Spectral Collocation Method with Adaptively Transformed Chebyshev Grid Points, *SIAM Journal of Scientific Computing* **28** (2006) 1798–1811.

[76] K.E. Teigen, P. Song, J. Lowengrub, A. Voigt, A diffuse-interface method for two-phase flows with soluble surfactants, *Journal of Computational Physics* **230** (2011) 375–393.

[77] L.N. Trefethen, M. Embree, *Spectra and pseudospectra: The behavior of nonnormal matrices and operators*, Princeton University Press, 2005.

[78] B.P. Tullis, S.J. Wright, Wetting front instabilities: a three-dimensional experimental investigation, *Transport in Porous Media* **70** (2007) 335–353.

[79] C.V. Verhoosel, M.A. Scott, T.J.R. Hughes, R. de Borst, An isogeometric analysis approach to gradient damage models, *International Journal for Numerical Methods in Engineering* **86** (2011) 115–134.

[80] S.M. Wise, J.S. Lowengrub, V. Cristini, An adaptive multigrid algorithm for simulating solid tumor growth using mixture models, *Mathematical and Computational Modeling* **53** (2011) 1–20.

[81] X. Ye, X. Cheng, The Fourier spectral method for the Cahn-Hilliard equation, *Applied Mathematics and Computation* **171** (2005) 345–357.

[82] J. Zhu, L.-Q. Chen, J. Shen, V. Tikare, Coarsening kinetics from a variable-mobility Cahn-Hilliard equation: Application of a semi-implicit Fourier spectral method, *Physical Review E* **60** (1999) 3564–3572.

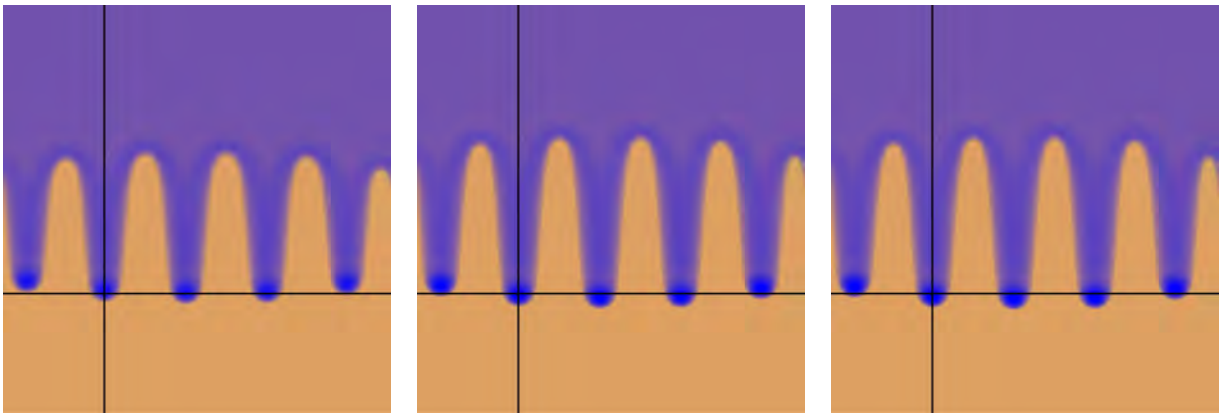

(a) 256^2 (b) 512^2 (c) 1024^2

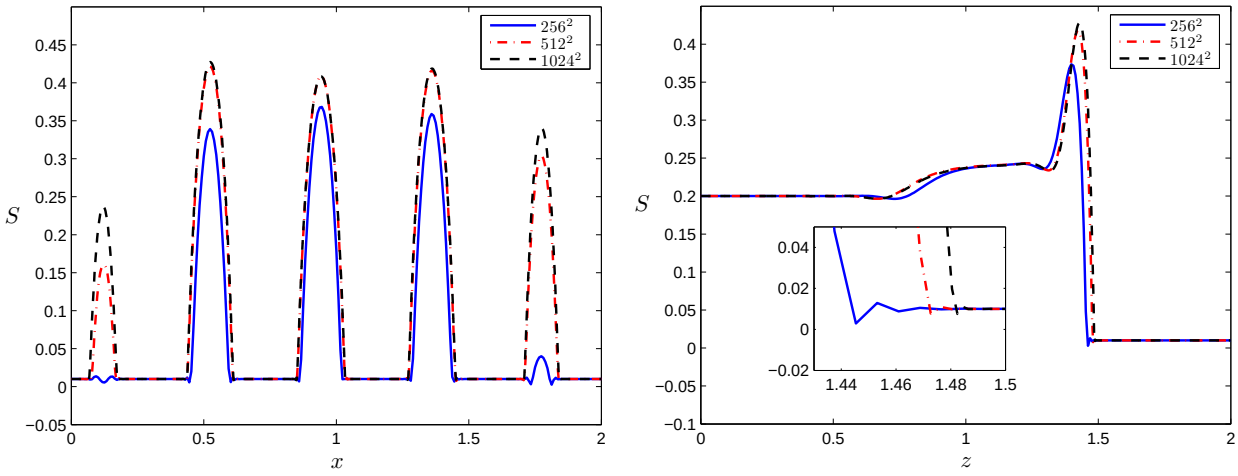

(d) Horizontal cutline (e) Vertical cutline

Figure 1: Convergence under grid refinement. We compute the saturation field at time $t = 147.5$ using grids of 256^2 (a), 512^2 (b), and 1024^2 (c) $\mathcal{C}^1$ quadratic elements. The solution is advanced in time with a small, constant time step, $\Delta t = 0.25$. The constitutive parameters are given by $\kappa = 50$, $\lambda = 4$, $m = 4$. The flow is defined by $N_{\mathrm{Gr}} = 20$, $S_0 = 0.01$, and $S_{\mathrm{in}} = 0.2$. The straight lines depicted in the plots (a)-(c) indicate the locations of the cutlines represented in (d) and (e). We observe that the saturation overshoot at the finger tips is underestimated on coarse meshes.

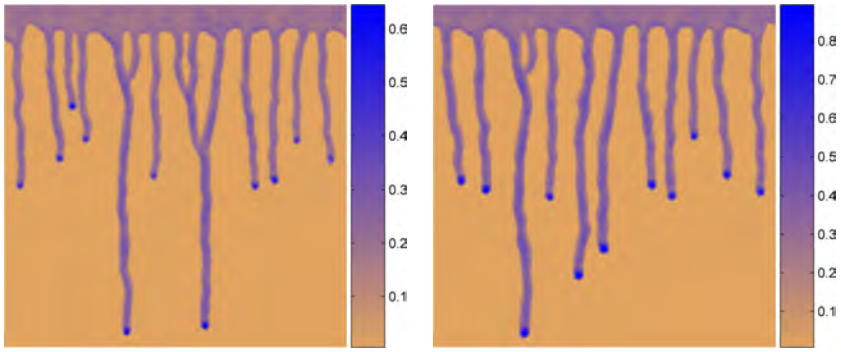

(a) $S_{\text{in}} = 0.2$

(b) $S_{\text{in}} = 0.3$

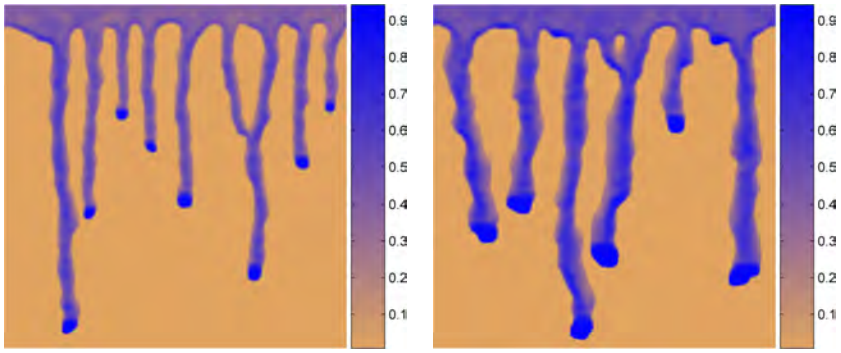

(c) $S_{\text{in}} = 0.4$

(d) $S_{\text{in}} = 0.5$

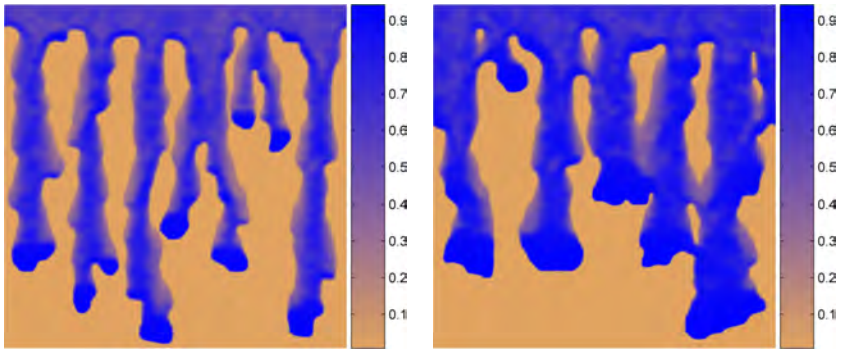

(e) $S_{\text{in}} = 0.6$

(f) $S_{\text{in}} = 0.7$

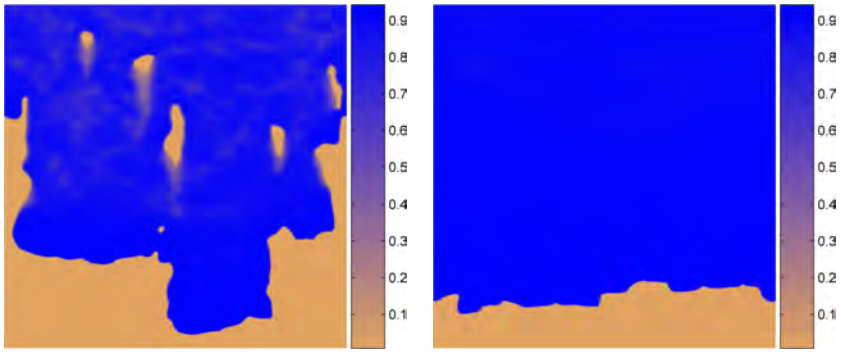

(g) $S_{\text{in}} = 0.8$

(h) $S_{\text{in}} = 0.9$

Figure 2: Flow patterns for various infiltration rates. The simulation set-up is in all cases identical, except for the imposed infiltration rate, which is controlled by varying the imposed saturation at the upper boundary, S_{in}. Low infiltration rates lead to multiple thin fingers with low saturation. Infiltration rates near the saturated conductivity induce a transition to a stable, compact front.

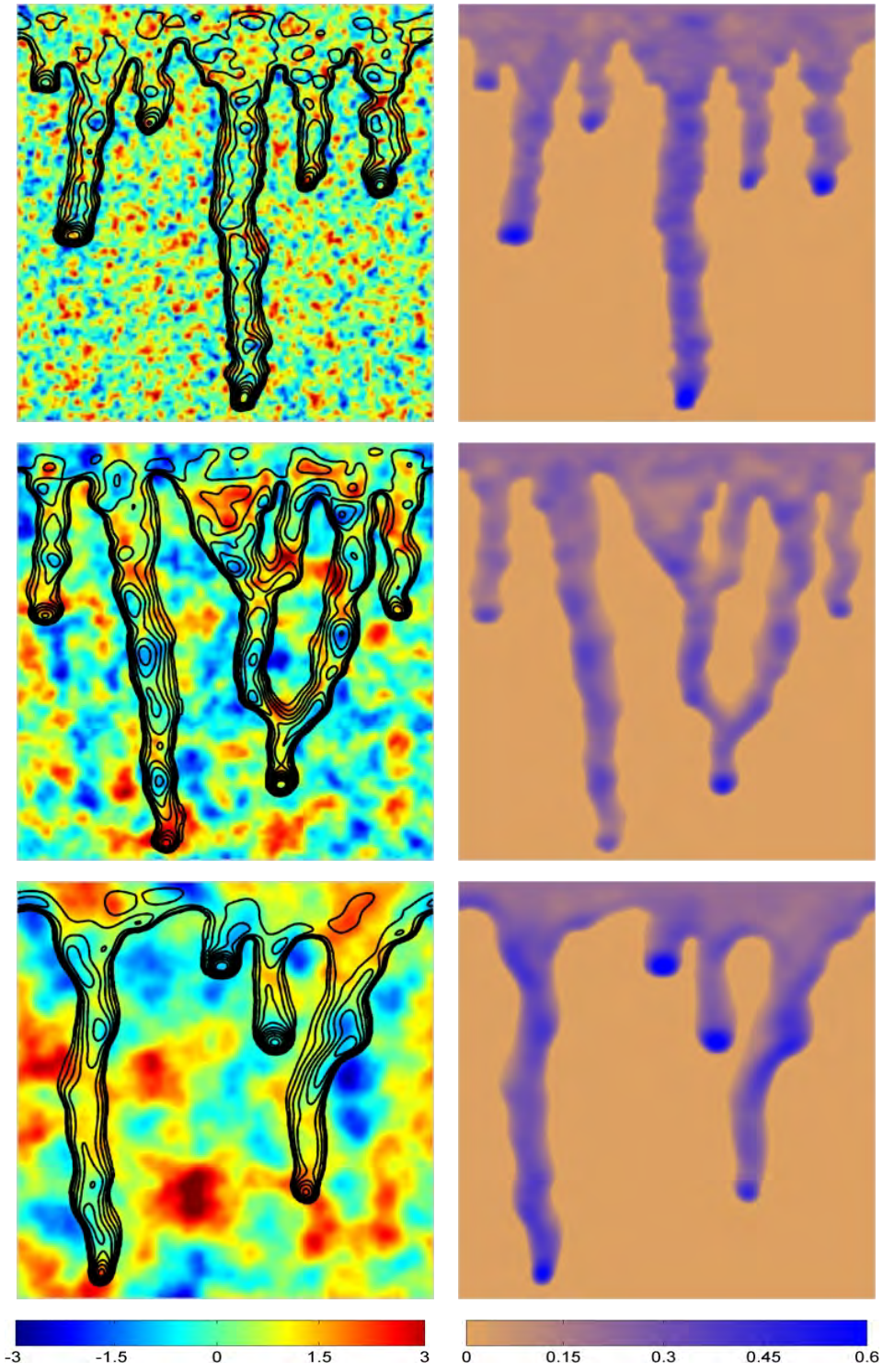

(a) Logarithm of permeability (b) Water saturation

Figure 3: Effect of heterogeneous permeability (I). Natural logarithm of the hydraulic conductivity (left) and water saturation (right). The permeability field was generated as a multivariate lognormal distribution with variance $\sigma^2_{\ln k} = 1$, and isotropic correlation length $l_x = l_y = l$. The first, second, and third rows correspond, respectively, to a permeability field with correlation length $l = h$, $l = 4h$, and $l = 8h$, where h is the mesh size. The simulations were carried out on a uniform mesh of 256^2 elements. Heterogeneity in the permeability induces meandering of the fingers, and affects the finger separation. Interestingly, there is a clear interaction between the correlation length of the permeability field and the typical finger length scale, which affects the intensity of flow focusing.

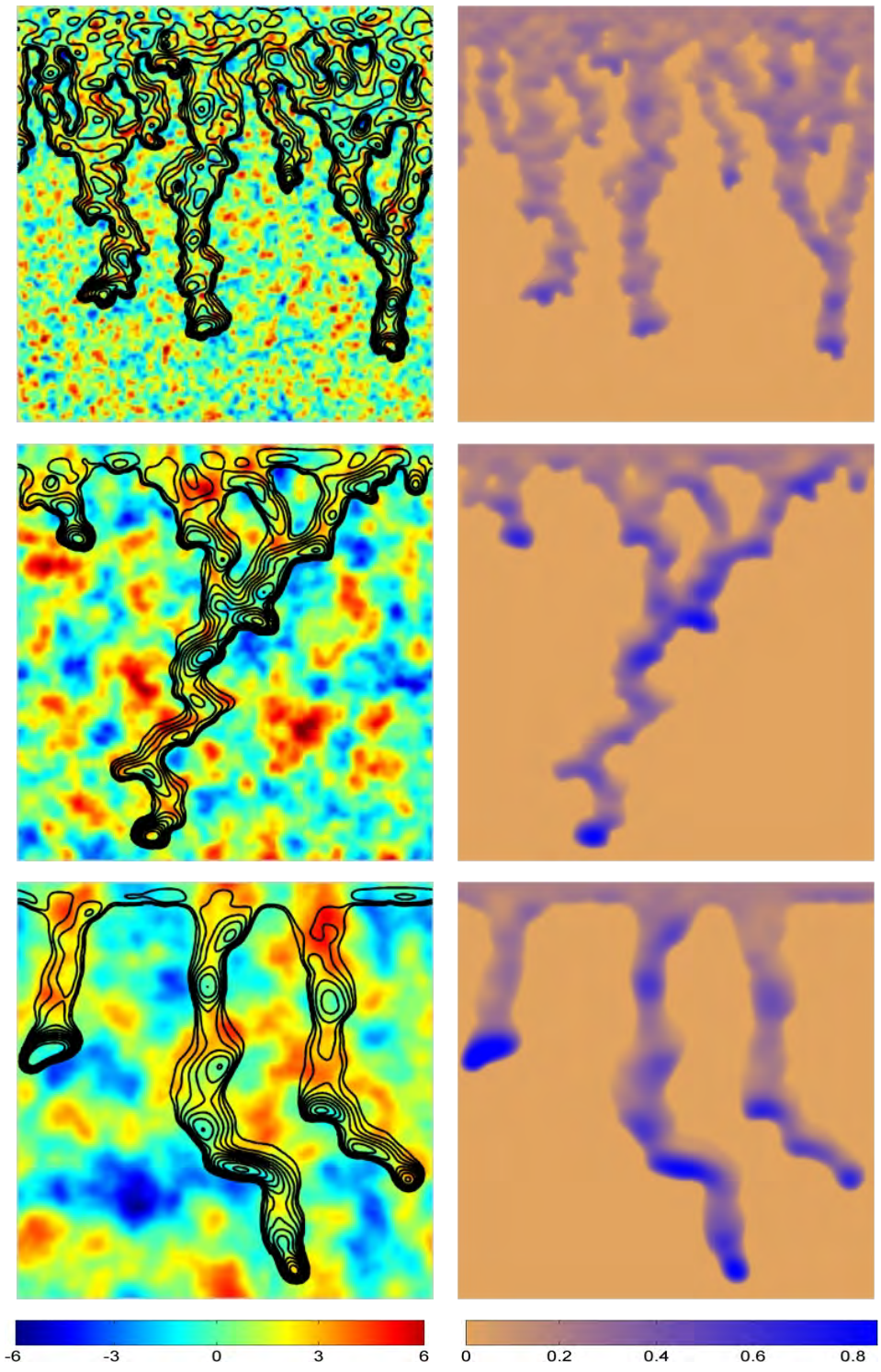

(a) Logarithm of permeability

(b) Water saturation

Figure 4: Effect of heterogeneous permeability (II). Same as Figure 3, but in this case the heterogeneity is stronger, with variance $\sigma^2_{\ln k} = 4$.

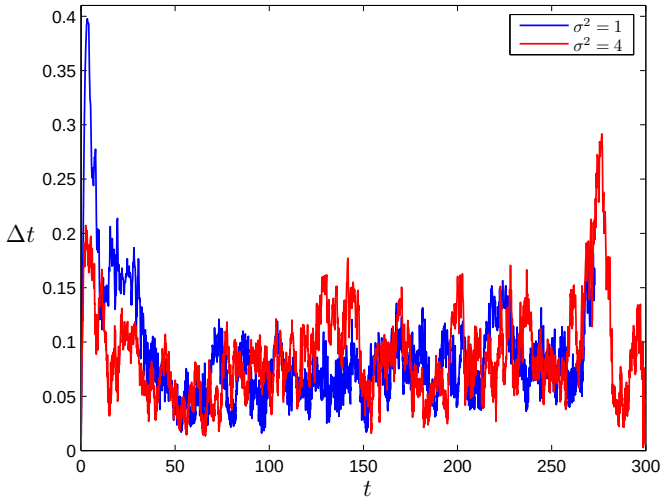

(a) $l = 1$

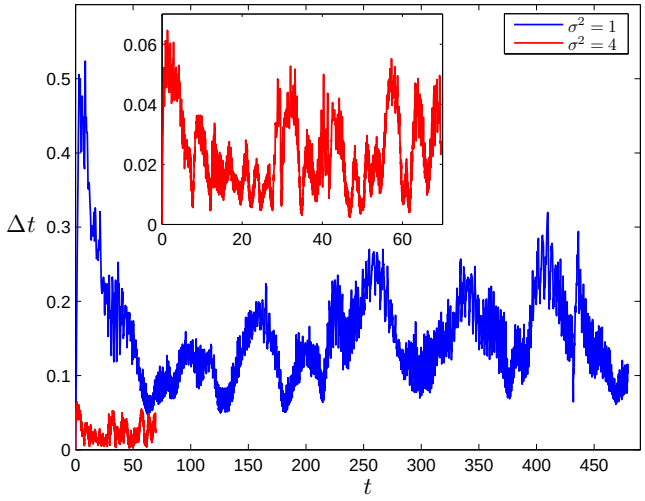

(b) $l = 4$

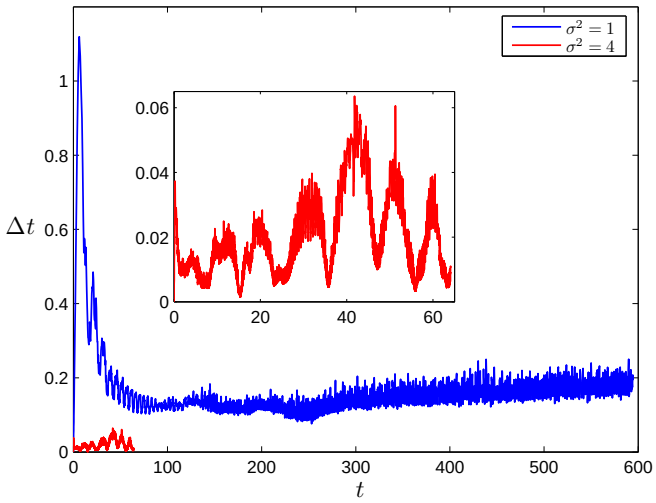

(c) $l = 8$

Figure 5: Time evolution of the time step size predicted by our adaptive algorithm for the simulations presented in Figures 3–4. The snapshot (a) corresponds to $l = h$, (b) to $l = 4h$ and (c) to $l = 8h$, where h is the mesh size. The plots indicate that the higher the variance of the permeability, the wider the range of relevant infiltration time scales. The plots also reveal that, for large correlation lengths ($l = 4h$ and $l = 8h$), heterogeneity accelerates the infiltration process, while for small correlation lengths ($l = h$), heterogeneity does not have a significant impact on the average infiltration velocity.

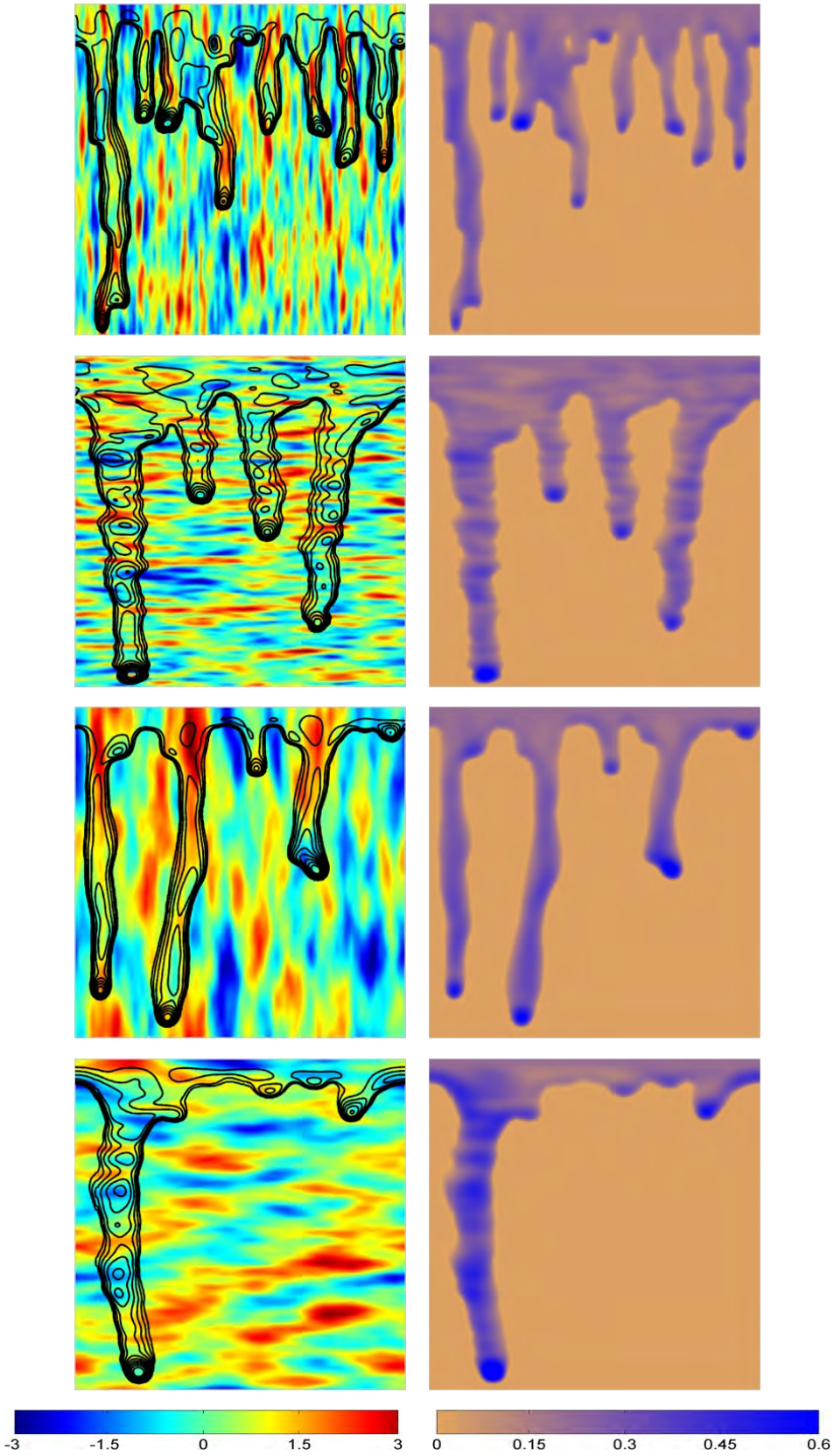

(a) Logarithm of permeability (b) Water saturation

Figure 6: Effect of anisotropy and soil structure (I). In these simulations, we model the impact of layering on the fingering instability. The permeability field was generated as a lognormal distribution with variance $\sigma^2_{\ln k} = 1$, and anisotropic correlation length, that is $l_x \neq l_y$. The first two rows correspond to $l_x = h$, $l_y = h$ and $l_x = h$, $l_y = 8h$, where h is the mesh size (vertical and horizontal layering, respectively, with small correlation length). The third and fourth rows correspond to permeability fields with larger correlation length, $l_x = 4h$, $l_y = 16h$ and $l_x = 16h$, $l_y = 4h$, respectively. The simulations were carried out on a uniform mesh of 256^2 elements.

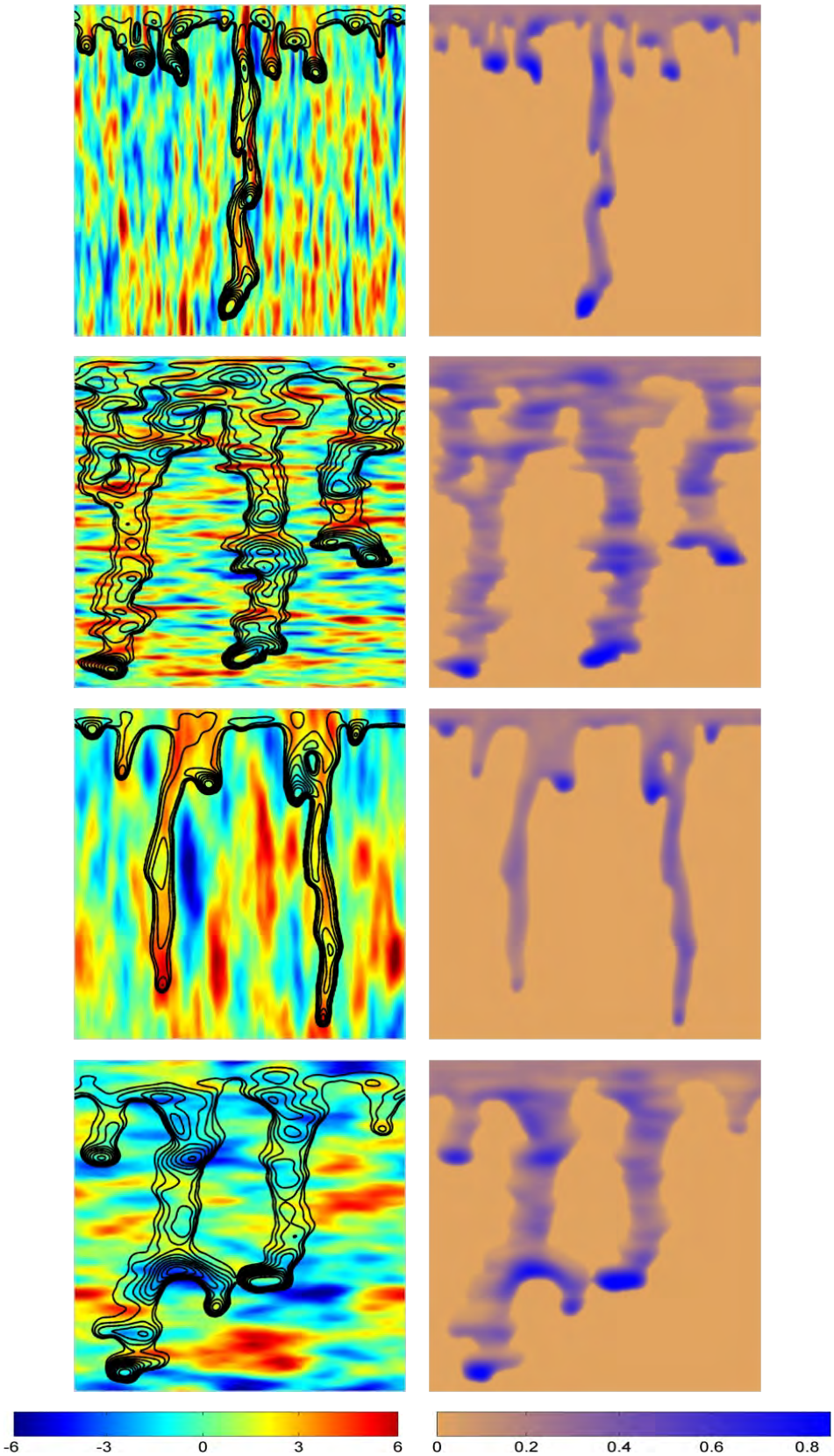

(a) Logarithm of permeability (b) Water saturation

Figure 7: Effect of anisotropy and soil structure (II). Same as Figure 6, but with a larger variance, $\sigma^2_{\ln k} = 4$.

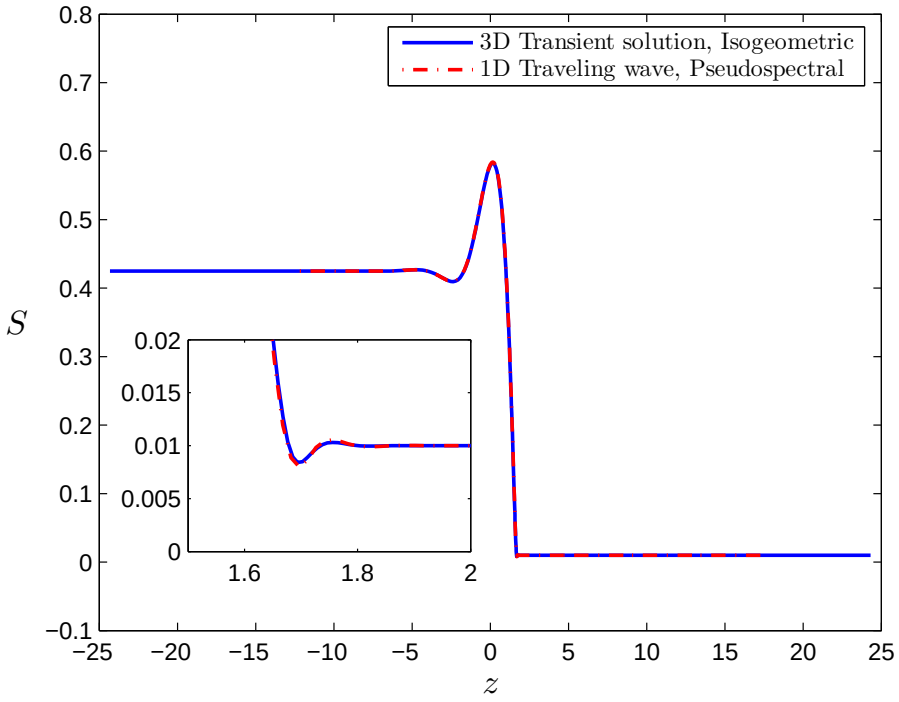

Figure 8: Traveling wave solutions to the infiltration theory computed as one-dimensional steady solutions on a moving frame of reference (blue, solid line) and as three-dimensional transient solutions of the infiltration theory (red, dashed line). The traveling wave solution has been computed using a rational pseudospectral method with adaptively transformed Chebyshev nodes, while the transient solution has been calculated using our three-dimensional code and the algorithms presented in this paper. The solutions are indistinguishable at the scale of the plot. The inset shows that both methods capture correctly the small undershoot located downstream of the wetting front.

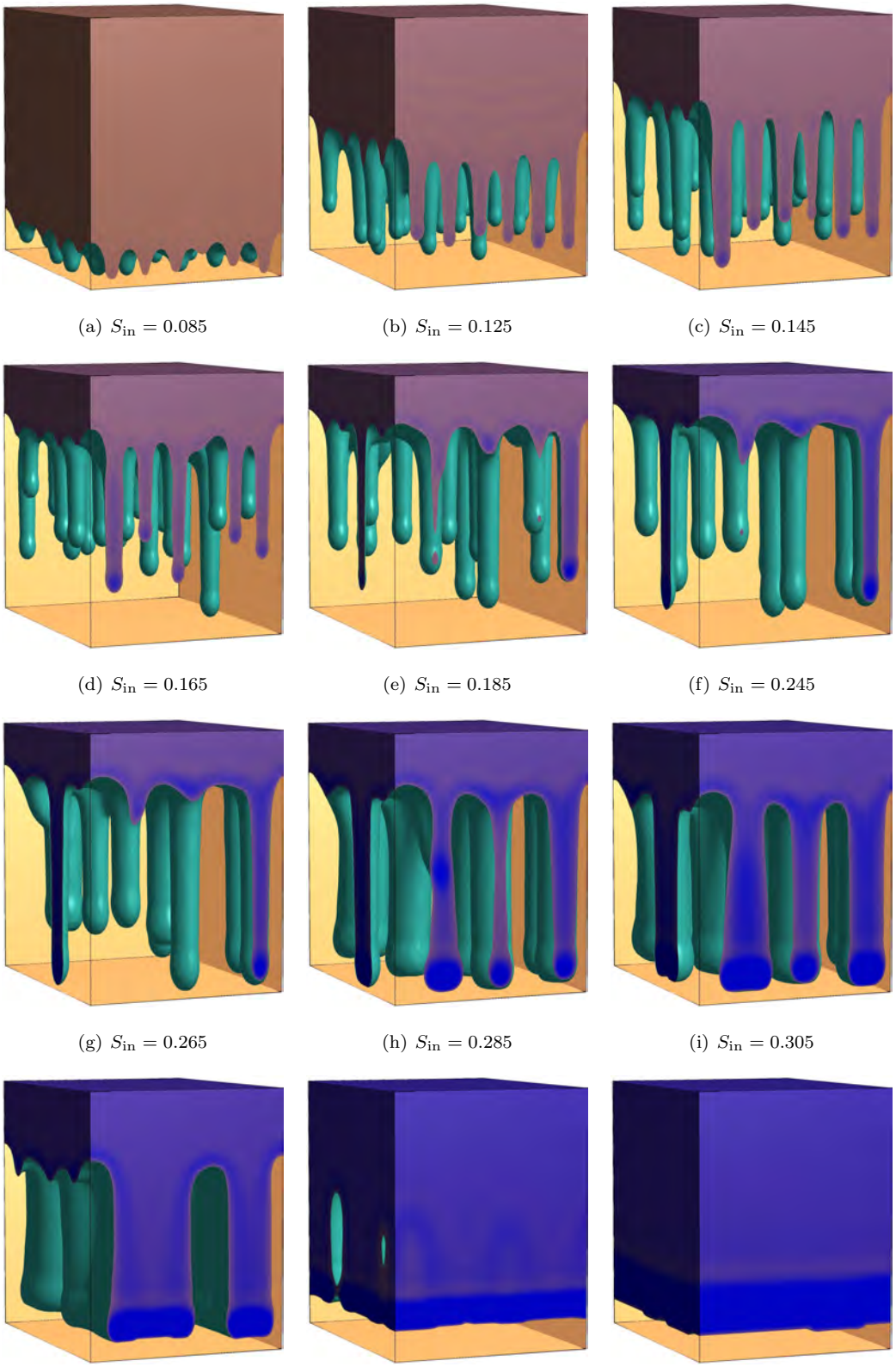

(a) $S_{\text{in}} = 0.085$ (b) $S_{\text{in}} = 0.125$ (c) $S_{\text{in}} = 0.145$

(d) $S_{\text{in}} = 0.165$ (e) $S_{\text{in}} = 0.185$ (f) $S_{\text{in}} = 0.245$

(g) $S_{\text{in}} = 0.265$ (h) $S_{\text{in}} = 0.285$ (i) $S_{\text{in}} = 0.305$

(j) $S_{\text{in}} = 0.325$ (k) $S_{\text{in}} = 0.345$ (l) $S_{\text{in}} = 0.365$

Figure 9: Three-dimensional simulations of water infiltration into a porous medium. The plots show isosurfaces of water saturation computed on a mesh of 128^3 quadratic elements. The flow is initialized with a perturbed flat wetting front at a distance 0.1 of the top of the domain. The wetting front moves downwards due to the action of gravity and capillarity, developing the so-called fingering instability for certain values of the infiltration ratio, which in our simulations is determined by the value of S_{in}. Each subfigure corresponds to a different value of S_{in}, as indicated in the labels that accompany the subplots.

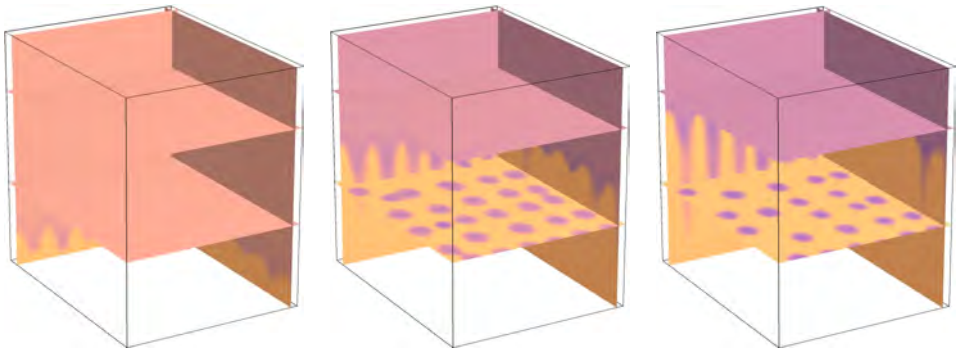

(a) $S_{\text{in}} = 0.085$ (b) $S_{\text{in}} = 0.125$ (c) $S_{\text{in}} = 0.145$

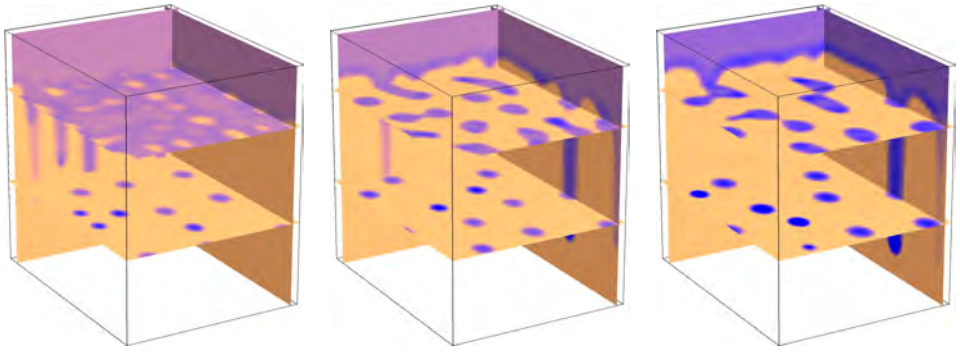

(d) $S_{\text{in}} = 0.165$ (e) $S_{\text{in}} = 0.185$ (f) $S_{\text{in}} = 0.245$

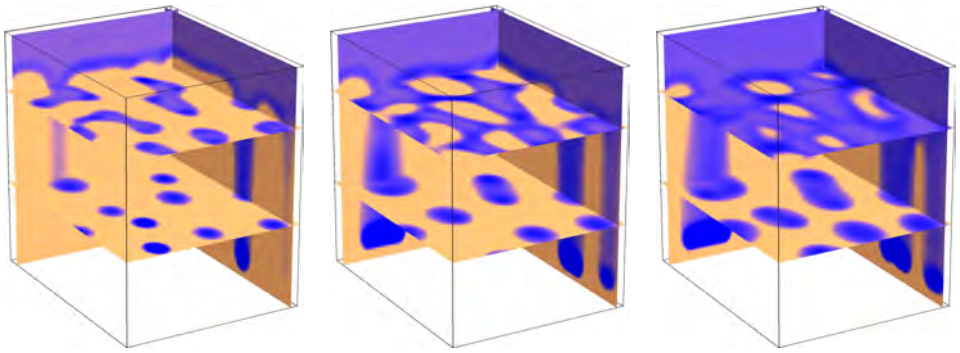

(g) $S_{\text{in}} = 0.265$ (h) $S_{\text{in}} = 0.285$ (i) $S_{\text{in}} = 0.305$

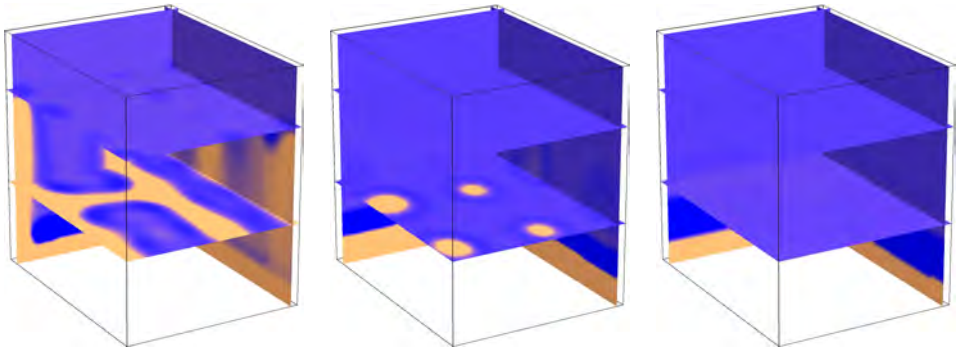

(j) $S_{\text{in}} = 0.325$ (k) $S_{\text{in}} = 0.345$ (l) $S_{\text{in}} = 0.365$

Figure 10: Three-dimensional simulations of water infiltration into a porous medium. The plots show slices of the solution across horizontal and vertical planes. The computational mesh comprises 128^3 quadratic elements. The flow is initialized with a perturbed flat wetting front at a distance 0.1 of the top of the domain. The wetting front moves downwards due to the action of gravity and capillarity, developing the fingering instability for certain values of the infiltration ratio, which in our simulations is determined by the value of S_{in}. Each subfigure corresponds to a different value of S_{in}, as indicated in the labels that accompany the subplots.

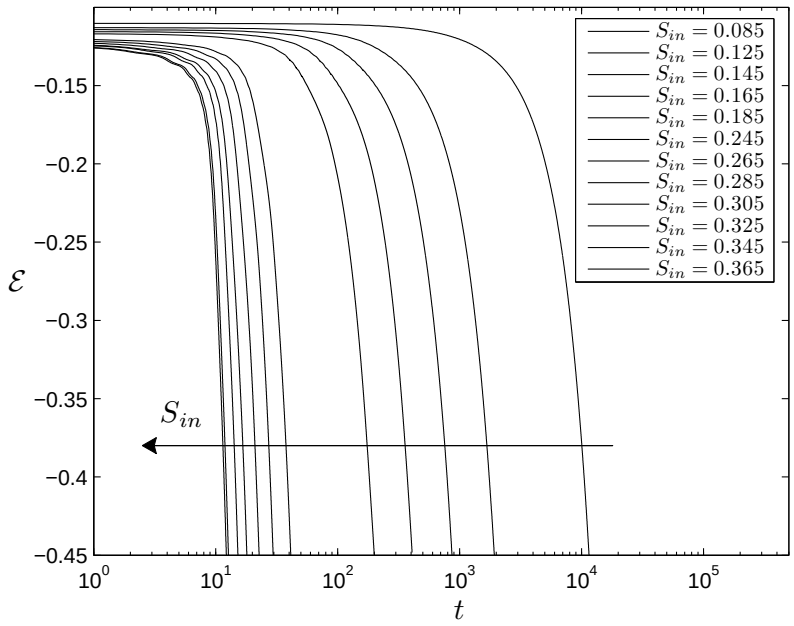

Figure 11: Time evolution of the free-energy functional $\mathcal{E}$ for a three-dimensional computation of gravity-driven infiltration. The plot shows that the free energy is time-decreasing, and thus, the algorithm respects the fundamental stability property of the theory for the space-time computational mesh employed in this calculation.